LARGE SPACECRAFT MEDIUM VOLTAGE DC (MVDC) POWER AND PROPULSION SYSTEM

A Thesis
Submitted to the Graduate Faculty
of the
North Dakota State University
of Agriculture and Applied Science

By

Sarah Talebzadeh

In Partial Fulfillment of the Requirements
for the Degree of
MASTER OF SCIENCE

Major Department:
Electrical and Computer Engineering

April 2024

Fargo, North Dakota

North Dakota State University
Graduate School

Title

LARGE SPACECRAFT MEDIUM VOLTAGE DC (MVDC) POWER AND PROPULSION SYSTEM

By

Sarah Talebzadeh

The Supervisory Committee certifies that this ***disquisition*** complies with North Dakota State University's regulations and meets the accepted standards for the degree of

MASTER OF SCIENCE

SUPERVISORY COMMITTEE:

Dr. Omid Beik
Chair

Dr. Di Wu

Dr. Chad Ulven

Approved:

04/09/2024
Date

Dr. Benjamin Braaten
Department Chair

ABSTRACT

This thesis introduces a medium voltage direct-current (MVDC) system for large spacecrafts with megawatt (MW)-scale power and propulsion systems for interplanetary transport. The proposed MVDC system comprises a nuclear electric propulsion (NEP) powered permanent magnet generator, a solar photovoltaic (PV), a backup battery energy storage system (BESS), an electric thruster, AC/DC loads, and the spacecraft low-voltage DC (LVDC) power system. The NEP is the main power source for the thruster, while the solar PV and BESS support payload and low-voltage systems. The energy sources are connected to the MVDC bus through power electronics converters. Unidirectional boost DC-DC converter and bidirectional boost DC-DC converters are adopted on the PV and BESS sources, respectively, while an isolated DC-DC converter is used to provide power to the thruster. To attenuate external disturbance and enhance the robustness of the proposed MVDC system, uncertainty and disturbance estimator (UDE) based controllers are designed for the power electronics converters in the MVDC system.

ACKNOWLEDGMENTS

The accomplishment of this thesis would not be possible without the help and support of my supervisor Dr. Omid Beik. First, I would like to express my deepest gratitude to him for the chance to work on an exciting research topic and for his support and guidance with patience. I am also grateful to my dissertation advisory committee members: Dr. Di Wu and Dr. Chad Ulven for their generous support and insightful suggestions.

I would like to acknowledge my friends Ms. Ghazaleh Sarfi and Ms. Mahzad Gholamian who have closely worked with me since the start of my M.Sc. journey and helped me fit in a new country.

I extend my heartfelt gratitude to my friends and colleagues at John Deere Intelligent Solutions Group, including Dr. Long Wu and Mr. Tyler J. Duffy. Additionally, I am thankful to Dr. Scott C. Johnson, Dr. Yuheng Wu, Mr. Yujiang Wu and Mr. Randy Worrel for their invaluable assistance in enriching my knowledge of engineering research through our collaborative work on numerous compelling projects.

Special thanks to my parents and my brother for all the support, understanding, and accompany, which gives me the courage to pursue my dreams.

Finally, I am extremely thankful to the ECE department of North Dakota State University for providing an ideal environment for my graduate studies here. The two peaceful and wonderful years at Fargo, ND were the most unforgettable experience of my life.

DEDICATION

I dedicate this thesis to my beloved family,

Nazila Nikoukar, Hamid Talebzadeh, and Shayan Talebzadeh

TABLE OF CONTENTS

LIST OF TABLES

LIST OF FIGURES

LIST OF ABBREVIATIONS

EPS.....Electrical Power System

PV .....Photovoltaic

RTG.....Radioisotope thermoelectric generator

PTV .....Pre-Transmission Validity

CEV.....Command Execution Verification

LEO.....Low Earth Orbit

MEO.....Medium Earth Orbit

GEO .....Geostationary Earth Orbit

ISS.....International Space Station

NEP .....Nuclear Electric Propulsion

NTP .....Nuclear Thermal Propulsion

iRosa .....ISS Roll-Out Solar Arrays

SAW.....Solar Array Wings

PVM.....Photovoltaic Module

MVDC.....Medium voltage DC

BESS .....Battery Energy Storage System

SAB.....Single Active Bridge

DAB .....Dual Active Bridge

PSFB .....Phase Shift Full Bridge

CCM.....Continuous Conduction Mode

HF .....High-frequency

LF.....Line-frequency

LIST OF APPENDIX TABLES

1. INTRODUCTION

1.1. Motivation

The prospect of interplanetary travel, particularly the ambitious goal of human missions to Mars, stands as one of the most significant challenges in modern space exploration [1]-[3]. While the allure of the Red Planet has captivated the imagination of scientists and engineers alike the journey to Mars presents obstacles, not least of which is the need for robust and reliable power and propulsion systems capable of supporting such long-duration missions. The concept of manned Mars missions has been the subject of extensive study and speculation [4]-[7]. The literature reveals a notable gap in the comprehensive understanding and development of power systems suitable for such monumental undertakings. These studies offer valuable insights into the challenges and potential solutions, but they predominantly concentrate on small spacecraft and focus on the nuances of short-term missions. While this is instrumental in advancing our understanding of space travel it falls short of addressing the multifaceted and intricate demands of a manned mission to Mars. Specifically, these works do not thoroughly explore the development and integration of robust, high-efficiency power systems capable of supporting not just the journey to Mars but also the sustained human presence and operations on the Martian surface. It is within this critical context that the current research seeks to bridge the gap, shifting the paradigm from small, unmanned craft to the more complex, long-duration habitats that manned missions necessitate. By addressing the limitations of existing literature and focusing on the scalability, reliability, and efficiency of power systems, this study endeavors to lay a more concrete foundation for the future of human interplanetary travel [8].

1.2. The State-of –the-Art of Spacecraft Power System

Spacecraft has several major subsystems, all these parts themselves may have backups in case of failure just to ensure that the missions will succeed. A Spacecraft Electrical Power System (EPS) is one of the fundamental and critical subsystems of a spacecraft, designed to generate, store, distribute, and manage electrical power throughout the entirety of a mission [9]. The EPS ensures the continuous operation of onboard systems, instruments, and life support systems, essential for mission success and crew survival in manned missions. It typically encompasses energy generation sources (commonly solar panels), energy storage units, power conditioning and conversion hardware (such power electronics converters), and power distribution networks. The EPS is engineered to operate in the harsh environment of space, characterized by extreme temperatures, vacuum, and radiation. It is designed to be highly reliable, efficient, and resilient, ensuring that the spacecraft remains operational over long durations.

To manage the electrical power in the spacecraft an EPS is required. The EPS provides an electrical structure for generation, storing, distribution, control, operation, monitoring and protection of the electrical power inside the spacecraft. Figure 1 is an overview of each main component [9].

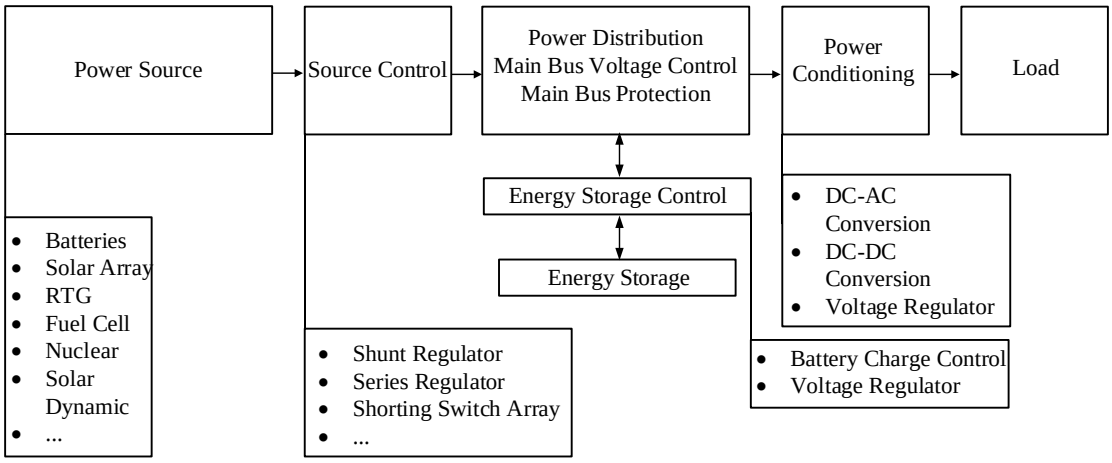

Figure 1. General structure of a spacecraft EPS.

According to the power levels and mission durations the optimum energy sources can be chosen for the power system. There are many power and propulsion system options available according to the planned mission such as solar photovoltaic (PV) cells, fuel cells, radioisotope thermoelectric generator (RTG), batteries, and nuclear power. Based on the mission final selection of the power source would meet multiple criteria [10]-[11]. The spacecrafts used as satellites orbiting the earth and other small spacecrafts with power levels below 10 kW primary batteries, solar PV, fuel cells, and RTG have been proposed as viable energy sources. Chemical-based propulsions can be scaled for megawatts (MW)-scale spacecraft propulsions in missions with relatively short durations. The PV solar sources may be used for long-duration missions with mid-range power levels and voltages up to 200 V; for instance, the ISS generates 105 kW using solar arrays [12]-[13].

However, the solar PV systems are limited to power levels below 200 kW, they are not readily scalable, and impractical where sun's reach is limited, e.g. the solar irradiance on Mars is about 590 W/m^2 while this is 1366 W/m^2 on Earth, and for farther distances the solar irradiance further reduces [14]. The power should be double of the power on Earth when reaching Mars [15].

$$\frac{G_1}{G_2} = \frac{P_2}{P_1} \tag{1}$$

Where G_1 and G_2 are the irradiances (in W/m^2), and P_1 and P_2 are the resultant power when irradiance changes (in W).

A spacecraft control system is used to operate a spacecraft from the ground. The source control covers the requirements of the whole mission, including support to preparing operations, besides the spacecraft operations themselves; it can also cover the ground-system operations [16]. The control systems consist of a computer system connected to one or more ground stations being utilized in communication. Some of the main functions of the control source are:

- Monitoring telemetry parameters to check that they are either within certain ranges or that they have certain expected values.
- Commanding of the spacecraft; typically, the sending of a command will involve Pre-Transmission Validity (PTV) checks to verify that the command is permitted, and Command Execution Verification (CEV) to ensure that the command has been executed properly onboard. Such checks are typically made by examining telemetry parameters, e.g. to be sure that a heater has been turned on following a switch-on command. Commands may be sent manually or automatically. In manual commanding, the spacecraft controller will send commands from an application called the 'manual stack': this is, in effect, a list of commands prepared on a special display which are sent by 'popping' them off the top of the stack. In automatic commanding, a schedule of commands (in effect a list with times assigned) is sent automatically by the system.
- Collecting data in history files, for later analysis or display.
- Alarm facilities to draw the attention of operations staff to anomalies: typically, an out-of- limits or another type of failed check will result in an audible and visible alarm, which requires explicit acknowledgement by the operator.
- Security facilities, to prevent unauthorized external access to the system and to control access to the various functions of the system within the control team; the limiting of access to commanding function is a typical example.
- Facilities to set up and maintain the spacecraft database, which describes the characteristics of the telemetry data, telecommand and other mission data.
- These are often referred to as 'mission-preparation facilities'.

Every electrical or electronic component on a spacecraft may be switched on or off via command. This has been done by using solid-state or mechanical relays that connect or disconnect the component from the common distribution circuit, called a main bus.

Power distribution system has multiple subsystems and a reconfiguration management unit. There are regulators for solar arrays, and charge and discharge regulators for batteries, power distribution unit, reconfiguration unit, constant and pulsive loads [17].

On some spacecraft, it is crucial to power off some components before switching others on to keep the electrical load within the limits of the supply. Voltages are mostly measured and telemetered from the main bus and currents are measured and telemetered from spacecraft components to show their consumption. A shunt-type regulator maintains a constant voltage from the power source. The input voltage of the shunt regulator is generally variable but higher than the spacecraft's required constant bus voltage. The shunt regulator converts excess electrical energy into heat, most of this heat is radiated away into space by radiating plates. On spacecraft with solar panels, it is desirable to off-point the panels from the sun exposure to control the heat for reducing the regulator input voltage. The focus of this paper is the electrical power system, i.e., the components and elements from the electric generator to the MVDC power system.

1.2.1. Existing Design and Criteria

When it comes to choosing an optimal EPS for the spacecraft some criteria should be considered as the following [9]. For creating an optimal spacecraft, several key elements need to be considered. Firstly, the top-level requirements must be identified, encompassing customer requirements, payload requirements, mission lifetime, mission profile, and environments. By analyzing these aspects, a comprehensive understanding of the spacecraft's needs emerges, leading

to the establishment of crucial electrical power profiles. As an example, Figure 2 shows the requirements for the NASA spacecraft.

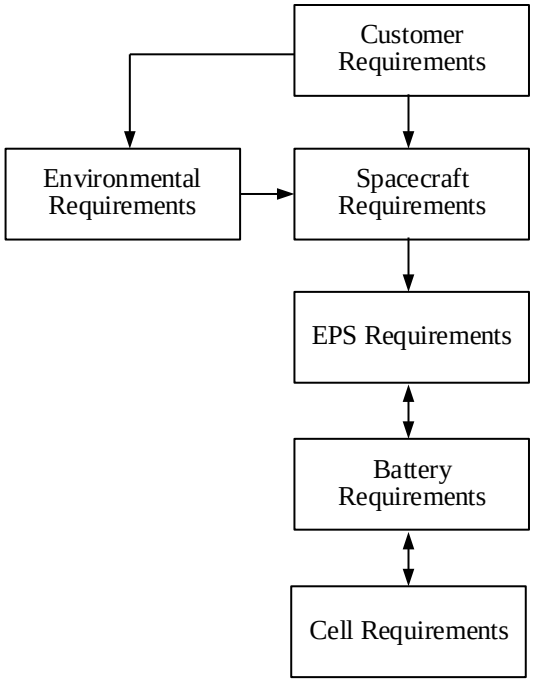

Figure 2. Requirements for spacecraft criteria [9].

The selection and sizing of the EPS involves assessing load power requirements, spacecraft configuration, and end-of-life power considerations. Through an evaluation process, the requirements for the electrical power system, such as choosing an optimal power source are derived, ensuring an optimized and efficient power supply [18]. The selection and sizing of the energy source are crucial, considering factors like orbital parameters, average power, eclipse time, and peak power. These considerations lead to the precise battery requirements, ensuring a dependable and sufficient power source throughout the spacecraft's mission.

To maintain optimal performance, power regulation and control must be addressed. This entails accommodating thermal control requirements, mission load requirements, voltage regulation control, and power source selection. By carefully managing these aspects, the electrical power system, battery, and cell requirements are effectively established, providing a robust and

controlled power infrastructure [19]-[20]. Through careful requirement identification, system selection, and power regulation, a remarkable spacecraft emerges. It features an impeccable electrical power profile, precisely sized power systems, mission-specific energy sources, and advanced power regulation and control. This harmonious combination empowers the spacecraft to venture into space with exceptional efficiency.

1.2.2. International Space Station (ISS) as Benchmark

1.2.2.1. Overview

The International Space Station (ISS) is the largest modular space station currently in LEO. This spacecraft project involves five participating space agencies: NASA (United States), Roscosmos (Russia), JAXA (Japan), ESA (Europe), and CSA (Canada). The ISS main job is to be a laboratory, observatory, while supplying transportation, preservation. LEO is being staged as a potential base for future missions to the Moon and Mars. In recent years, the ISS has been served for commercial, diplomatic, and educational purposes additionally. The ISS is a modular space station. Modular stations can allow modules to be added to or removed from the existing structure, allowing greater flexibility [21].

The ISS weighs about 420,000 kilograms. This is equivalent to more than 330 automobiles. It is 74 m long by 110 m wide. This is equivalent to a football field, including the end zones. The solar array surface area is 2,500 square meters, which is an acre of solar panels and enough to power 10 average sized homes with 110 kW of power [22]-[24]. It takes about 90 minutes for the ISS to circle Earth one time. During the daylight periods, temperatures reach 200ºC, while temperatures during the night periods drop to -200 ºC. Figure 3 shows the ISS configuration [25].

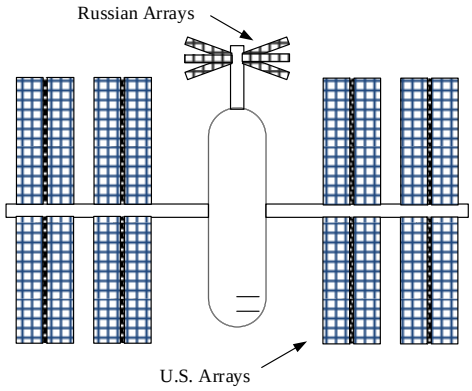

Figure 3. The ISS configuration.

The ISS has different parts such as structural trusses, pressurized habitation modules, photovoltaic solar arrays, docking ports, thermal radiators, experiment bays and robotic arms. The major ISS modules have been launched by America and Russian shuttles. Figure 4 shows the ISS with its components [26].

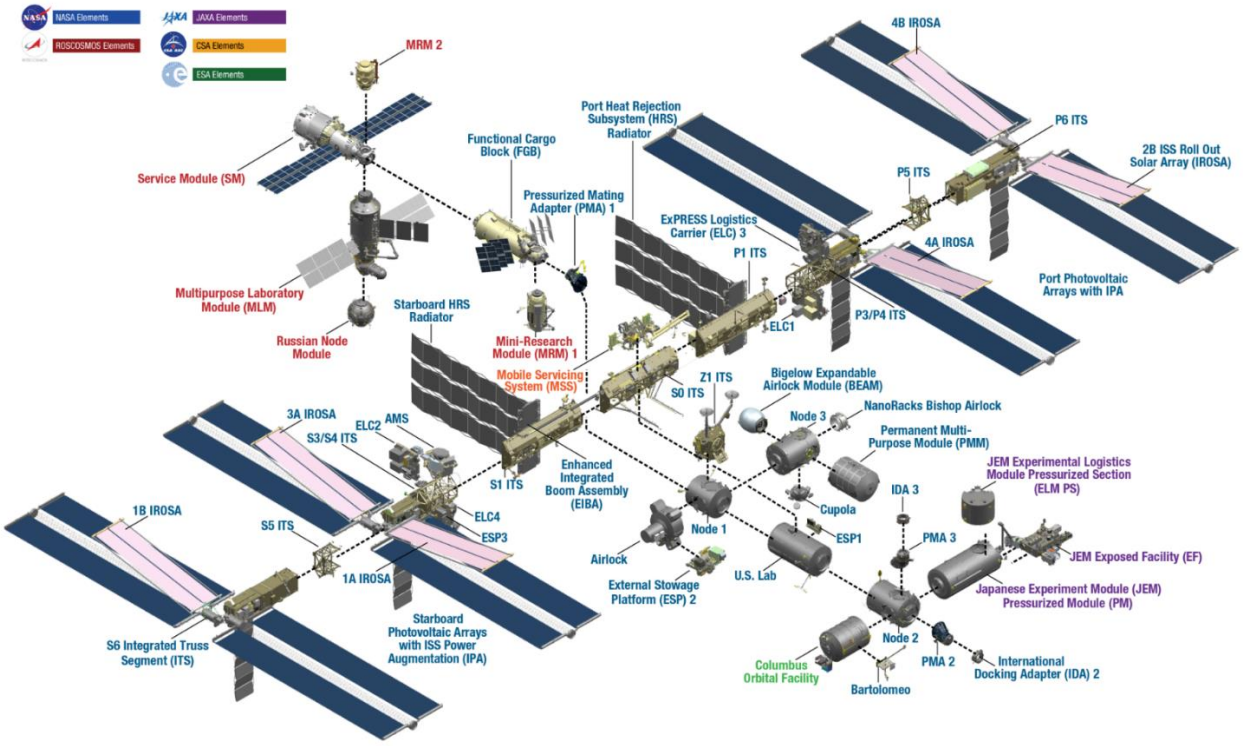

Figure 4. ISS components [27].

1.2.2.2. ISS EPS

The ISS EPS consists of two major segments: a 160-Volt U.S.-built portion, and a 28-Volt and 120-Volt Russian-built portion. The two systems are generally independent, but they are interconnected via dc converters, which allows mutual transfer of power. Solar panels directly convert sunlight to electricity. Large numbers of cells are assembled in arrays to produce high power levels. The ISS power system generates 105 kW using solar arrays. US modules (wings) generate most of the power, around 76 kW, for maintaining the ISS in the orbit and keeping its component working properly. Russian modules produce 29 kW power from their solar panels.

These U.S. solar arrays are configured into eight solar array wings (SAW) with two blankets per wing and two solar array wings per Photovoltaic Module (PVM) and a total of four PVM on ISS [28]. When completely extended, each is 35 meters in length and 12 meters wide. Each SAW can generate nearly 31 Kilowatts of direct current power. Each wing folds into a solar array blanket box just 51 centimeters high and 4.57 meters in length as it is retracted [29].

Figure 5 shows the layout of the eight arrays with the nomenclature used by the ISS program for labeling the eight SAWs (1A, 1B, 2A, 2B, 3A, 3B, 4A, and 4B) and the four PVM's (S4 and S6 on the starboard Truss and P4 and P6 on the port Truss). Each of the eight 11.7 m wide by 35.1 m long arrays are covered with 8 cm x 8 cm silicon solar cells laid out in 82 parallel strings with 400 cells in series per string. After the first solar panels have been launched to the space they were working indefinitely, therefore, their performance is decreasing yearly. NASA has deployed a new series of solar panels on the existing ones [30]. Six ISS Roll-Out Solar Arrays (iROSA) solar arrays augment the power drawn from the existing arrays on the ISS. These solar panels have been launched to space on SpaceX mission. Figure 6 shows how iROSA solar arrays are implemented.

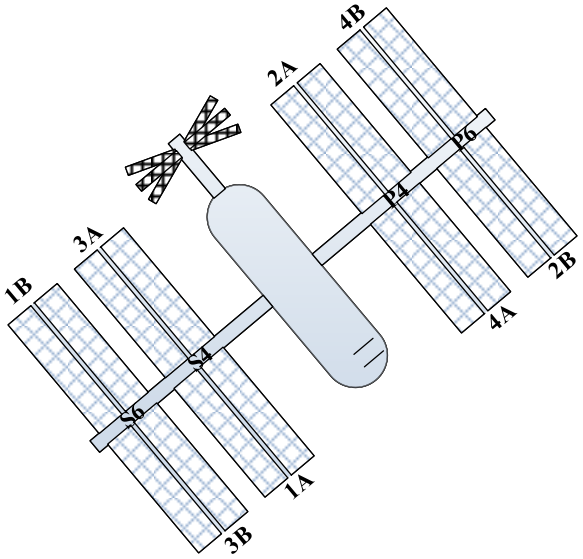

Figure 5. Configuration of ISS solar array.

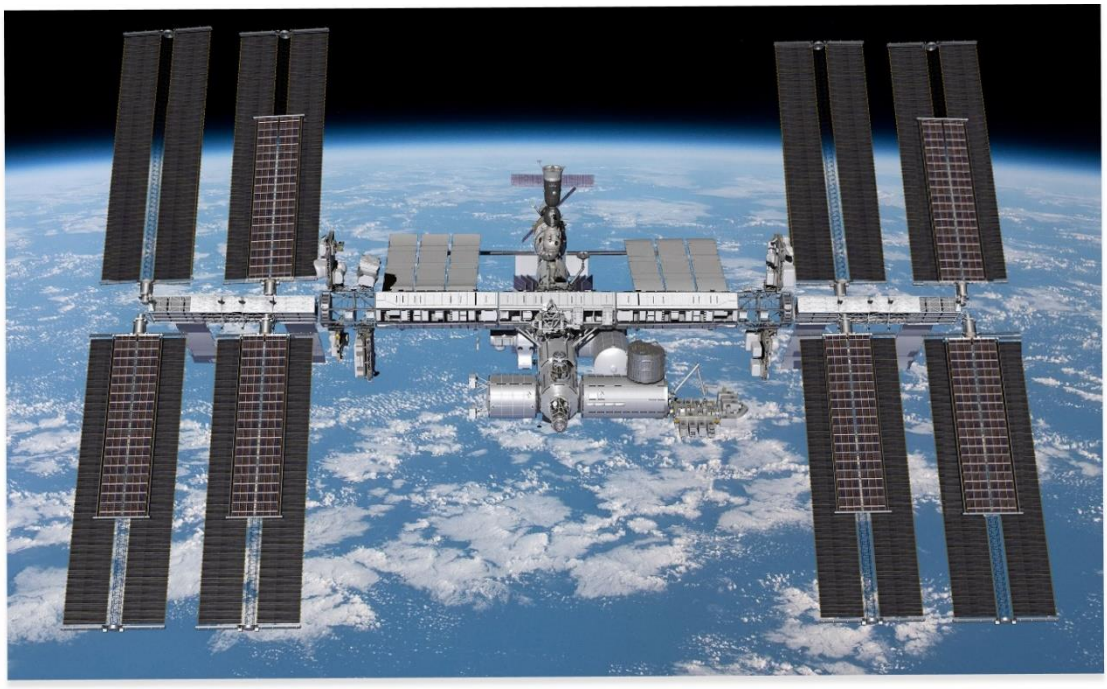

Figure 6. iRosa on ISS [30].

In general, double-sided solar arrays produce electrical power to the ISS, therefore, in these analyses only U.S. segments have been studied. These types of solar arrays are called bifacial cells. One side can collect direct sunlight and the other side can reflect the light off from the Earth. They

have better efficiency when operating at a lower temperature than single-sided cells commonly used on Earth.

The ISS is powered by a set of 160 V PVs in the US sector. The negative end of the arrays grounded to the conducting structure of the ISS. The solar arrays produce more power than the station needs since the power system needs to charge the batteries in time of eclipse. When the station is in sunlight, about 60 percent of the electricity that the solar arrays generate is used to charge the station's batteries. At times, some or all the solar arrays are in the shadow of Earth or the shadow of part of the station. This means that those arrays are not collecting sunlight. At these times the batteries are supposed to generate the power that the station needs.

The ISS originally used nickel-hydrogen batteries for energy storage as a backup for solar panels. In 2016, these batteries have been replaced with lithium-ion batteries [31]. One lithium-ion battery and corresponding adapter plate replaces two nickel-hydrogen batteries. After all the replacement that has been done 48 Ni-Hi batteries have been removed and now there are 24 Li-Ion batteries on the ISS [32]. Each channel has 3 Li-Ion batteries (In total ISS has 8 channels). Figure 7 indicates how the batteries are assembled into the station. The ISS has a variety of loads, or types of equipment, on board. Some of the main types of loads on the ISS include:

- Scientific equipment and experiments: The ISS has several facilities for conducting scientific research in a variety of fields, including biology, Earth science, astrophysics, etc.
- Life support systems: The ISS has several systems in place to provide a habitable environment for the crew, including oxygen generation, water recycling, and temperature control.
- Communications equipment: The ISS has several antennas and other equipment for communicating with the ground and with another spacecraft.

- Navigation and control systems: The ISS has a few systems for navigation, guidance, and control, including thrusters for adjusting the spacecraft's position and orientation.
- Crew quarters: The ISS has sleeping quarters, a galley, and a toilet for the crew to use while they are on board.
- Exercise equipment: The ISS has a few pieces of equipment, such as a treadmill and a stationary bike, to help the crew stay in shape while they are in space.

More information has been provided in Appendix Table A2.

The ISS serves as a benchmark for studying the integration of solar arrays and battery storage in this thesis. Their usage on the ISS, where continuous and reliable power supply is essential for human habitation, demonstrates their suitability for critical missions like a Mars expedition. By selecting the ISS solar arrays and batteries as a benchmark, valuable knowledge and operational experience gained from the ISS can be applied to inform the design and implementation of robust power systems for future Mars exploration. The well-documented performance, proven reliability, and suitability for continuous human habitation make the ISS power sources an ideal reference for designing efficient and resilient power supplies for Mars missions.

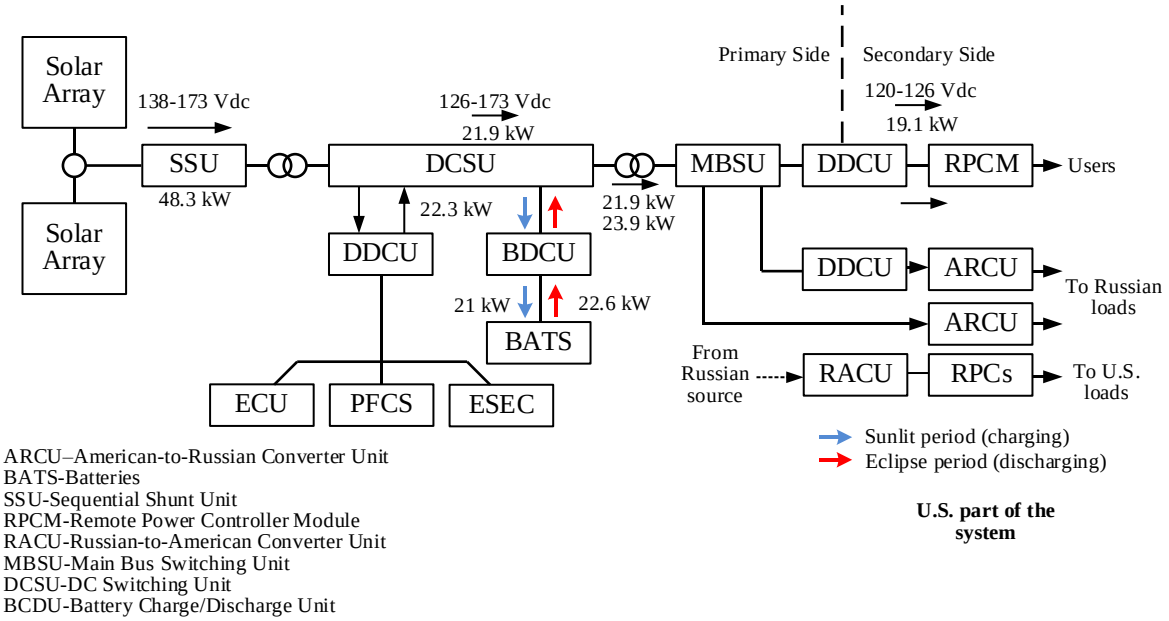

Figure 7. ISS batteries placement.

1.3. Challenges and Problem Definition

Various research put effort into the design of a spacecraft for Mars mission and its control algorithm to enhance stability, efficiency, and power quality [33]-[36]. However, challenges remain in the reliability improvement of the EPS. One of the primary challenges in designing efficient spacecraft power systems is considering the vast differences in distances and corresponding travel times to various celestial destinations. Understanding the distinct characteristics of spacecraft missions in Medium Earth Orbit (MEO), Geostationary Earth Orbit (GEO), and Low Earth Orbit (LEO) is essential in tailoring the design and requirements of their respective power systems. Missions within LEO typically range from about 160 to 2,000 kilometers above Earth's surface [37]-[41]. These missions usually involve activities like Earth observation, satellite imaging, and certain human-operated spaceflights. The duration of these travels often would be around minutes to a few hours. In contrast, MEO, located approximately 2,000 to 35,786 km above the Earth, is commonly used for navigation satellites, like those used in

GPS systems, where a balance between coverage area and signal strength is crucial. The highest of these orbits, GEO, at about 35,786 kilometers directly above the equator. This orbit is ideal for communications and weather satellites, requiring highly stable and reliable power systems due to their constant exposure to the harsher conditions of space, including solar radiation. Each orbit type, with its specific altitude and mission objectives, demands distinct considerations in terms of power generation, sustainability, and durability. These orbits are specific to Earth and are used to categorize the positions of artificial satellites around our planet. Figure 8 indicates the orbital altitude and coverage areas.

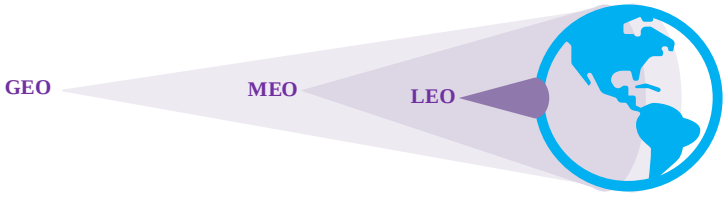

Figure 8. Schematic of the orbital altitude and coverage areas.

Missions to Mars involve interplanetary travel, departing from Earth's gravitational influence and navigating through space to reach the orbit of Mars, a journey of approximately 54.6 million km at its closest approach to Earth. encompasses significantly longer travel times, potentially takes several months. This journey is significantly more complex and lengthier than positioning satellites in Earth's orbit, involving intricate trajectory calculations, propulsion requirements, and energy management to cover the millions of kilometers between Earth and Mars.

All the spacecrafts that have been launched into space have made a huge development in our knowledge regarding space and deep space. However, the most challenging issue is the power system of the spacecraft [42]-[44]. Robust power system design that can provide the power to all the components at any time of the travel is vital. This system should be able to maintain the power level and have enough power to provide sufficient propulsion for the spacecraft to be launched

into space and orbit changing [45]-[47]. Studies have shown many different designs for spacecraft power systems for Mars mission. [48] investigated on a 500 W vertical axis wind turbine, ground-based, with focus on the atmosphere challenges. [49] studied wind turbines for uncrewed science missions as an alternative for power supply. Their conclusion is that wind power is a good alternative power supply for uncrewed missions. It should be emphasized that the power demand disparity between manned and unmanned missions is incredibly significant: Crewed Mars mission requires a net electric power of 80 kW to supply a six-person crew during a 500-sol mission [50]. This is much more power than required by an uncrewed mission, for example, the thermoelectric generator of MSL rover (Mars Science Laboratory) has been able to generate 0.11 kW of electrical power. Power generation on Mars missions is acritical topic in numerous studies. However, the discussion is mainly on short travels like LEO, or they only focus on uncrewed missions. Many contributions on power systems (focused on PV cells/panels) have been published [51]-[56]. However, the issue with solely using PV panel is the dust on Mars surface which drains the power from spacecraft.

The efficacy of solar panels in generating power is directly influenced by two critical factors: solar irradiance and temperature [57]. These factors undergo significant changes during a mission to Mars, impacting overall power generation. As a spacecraft travels from Earth to Mars, it experiences a decrease in solar irradiance, the intensity of the Sun's rays. This decrease is due to the increasing distance from the Sun; Mars orbits approximately 1.5 times farther from the Sun than Earth. Consequently, the amount of solar energy available for panels to convert into electricity is significantly reduced. Besides, a solar eclipse is a natural phenomenon that results in an abrupt and short-time perturbation of the solar radiation reaching the area of its visibility on the planet's surface. This phenomenon can reduce solar irradiance significantly, which leads to a decrease in

the power level of solar panel [58]. Solar panel performance is also sensitive to temperature changes. In space, the absence of atmospheric buffering leads to extreme temperature variations. Direct sunlight, the panels can become exceedingly hot, while the temperature can drop drastically in the shadow of a planet or during night-time on Mars. This factor makes solar panels unreliable. For such a long travel to Mars, in which the distance itself can reduce the irradiance, using only solar panels can be really challenging and less practical. Figure 9 indicates how power changes when temperature and irradiance are reducing.

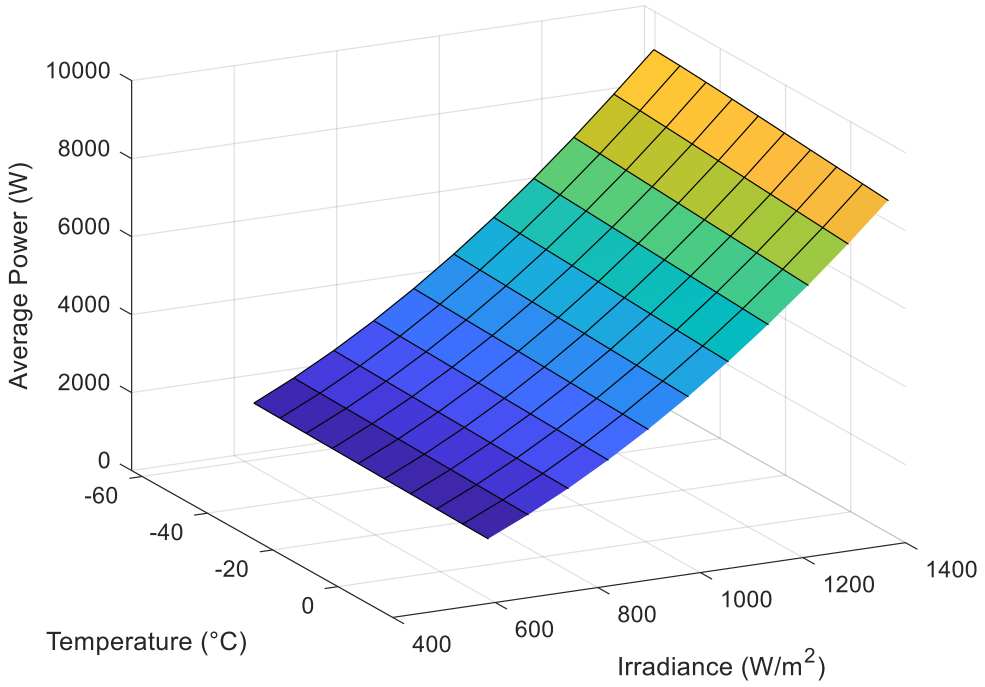

Figure 9. Solar panel power change.

Thus, in order to ensure the successful space missions to Mars, there are several challenges must be properly addressed:

1. Investigating proper power source to support the high-power demand of the space mission;
2. Implementing a high-power spacecraft power management and distribution (PMAD) system to meet the power needs of different subsystems;

3. Ensuring the stability and robust operation of the PMAD.

To address those challenges, in this work, first a high-power power system architecture is proposed for space missions (Figure 10). This spacecraft power system consists of 3 different energy sources, Solar panel, Batteries and Nuclear electric propulsion (NEP). All these sources are connected to the common bus bar through power electronics converters to supply the spacecraft loads and thrust. Second, different power electronics converter topologies have been reviewed and investigated to optimize the PMAD. Third, to enhance the reliability and robustness of the proposed PMAD, robust control algorithms are proposed for the power electronics converter that is used in the PMAD.

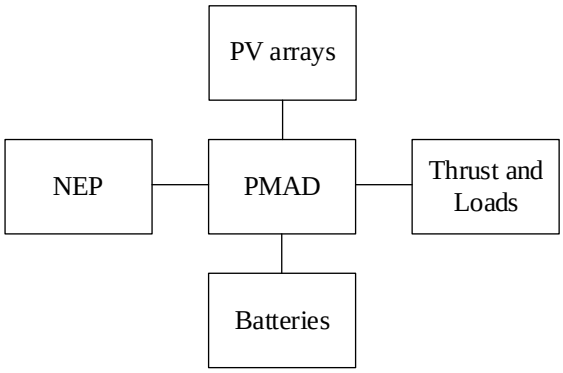

Figure 10. The proposed power system architecture for space missions.

1.4. Challenges and Contributions

The primary objective in designing a large spacecraft power and propulsion system capable of MW-level is to achieve a highly reliable, efficient, and robust system that can sustain long-duration space exploration. This involves the integration of advanced power sources, such as high-output solar arrays and nuclear reactors, with state-of-the-art energy storage solutions to ensure a consistent power supply. The system must incorporate PMAD technologies that facilitate optimal energy allocation to various subsystems, maintaining operational stability in the face of dynamic space environments and mission requirements. Additionally, the design must prioritize scalability,

fault tolerance, and adaptability to support a wide array of mission profiles and extend beyond the current frontiers of space travel. All components and systems will be engineered to meet rigorous standards of weight and volume efficiency, critical for launch viability and mission success, while also considering ease of maintenance, repair, and potential scalability for future enhancements or power needs adjustments. Challenges in designing a large spacecraft power system can be defined in 3 categories:

I. **Power Source**

One of the principal challenges in designing spacecraft power systems is the selection and integration of appropriate power sources that can sustain the high-power demands of long-duration space missions. Traditional power sources, such as solar panels, must be capable of generating significant amounts of energy while remaining lightweight and durable against the harsh conditions of space. Moreover, for long mission duration, alternative power sources like nuclear reactors become vital. The intricacy of incorporating these diverse power sources lies not only in their physical deployment but also in the efficient management and distribution of the energy they generate. Balancing the energy supply with the dynamic and sometimes unpredictable power demands of a spacecraft requires a sophisticated power management system that can adapt to varying conditions without sacrificing performance or safety.

II. **Spacecraft PMAD System**

The development of a high-power Spacecraft PMAD system poses a significant role in the path of deep space exploration. This system must seamlessly allocate energy to various spacecraft subsystems, which have different and often variable power requirements. For example, life support systems, scientific instruments, and propulsion units all have unique

energy needs that the PMAD must satisfy reliably. The challenge is compounded when considering the need to incorporate redundancy, fault tolerance, and the ability to adapt to failures or changes in the mission profile. Efficient power distribution is further complicated by the need for weight and space minimization, which restricts the amount of hardware that can be onboarded, thereby demanding innovative solutions that leverage advanced electronics and control systems.

III. Stability and Robust Operation

Maintaining the stability and robustness of the PMAD system is crucial for the success of space missions. Power systems in space are subjected to a variety of disruptions. The PMAD must be able to handle these perturbations while ensuring that the spacecraft's power supply remains stable and reliable. This involves developing advanced control algorithms that can anticipate and mitigate potential disturbances, as well as designing converters and other power electronic devices that can operate effectively under a wide range of conditions. Moreover, the need for the PMAD system to operate over long durations without maintenance increases the reliance on automated diagnostics and self-healing mechanisms to ensure continuous and uninterrupted power delivery.

For selecting power sources for a MW-level spacecraft system involves a multi-faceted approach that can meet the varied demands of long-duration missions. The NEP, PV arrays, and Batteries offers a comprehensive mix of energy generation and storage capabilities. Each of the power sources' benefits is described in Table 1.

Table 1. Advantages of Power Sources.

Power Sources	Benefits
NEP	High Power, Long-Term, Reliable energy for deep space missions.
PV arrays	Low-Power, Sustainability, and abundant energy during sunlight.
Batteries	Quick energy release for peak demands and energy storage for eclipse periods.

To make the power transmission between the energy sources and loads are ensured. The energy sources should be connected through power electronic converter to the common DC bus bar.

In order to integrate PV arrays with the spacecraft's power bus, boost converters are essential. These converters escalate the voltage from the PV arrays to the required level for the bus, thereby ensuring compatibility with the system's voltage standards and facilitating efficient power transfer. The heat generated by the nuclear reactor is converted into electrical power via a permanent magnet generator, which operates at a constant speed. This AC voltage is then converted to DC by a rectifier, allowing for connection to the common bus bar. The stable output from the rectifier also plays a pivotal role in regulating the bus voltage, thus maintaining a consistent power supply within the system.

Additionally, the required power from the battery is managed by a bidirectional boost converter. This advanced component not only steps up the voltage for discharge operations but also enables the recharging of the battery, providing an efficient energy storage solution.

To meet the high-power demands of the electric thruster, an Isolated DC-DC converter is employed. This converter boasts superior power density due to its galvanic isolation, which offers the dual benefits of electrical isolation and noise reduction. The implementation of this converter

is crucial for optimizing the power delivery to the electric thruster, ensuring that it operates at peak performance while mitigating risks associated with electrical interference.

1.5. Outline

This thesis is organized as follows:

- Chapter 2 discusses the proposed PMAD system. For providing enough power to the thrust, NEP has been used. Besides, PV and BESS are used to support the MVDC and meet the power demand. The power conversion between these 3 sources through DC common bus have been analyzed.
- Chapter 3 discusses the control approach for the PV and BESS side power electronics converters. The control approach of each converter has been analyzed. The model of each has been given.
- Chapter 4 will discuss how the load and thrust power would be regulated. A new control approach for the most effective regulation has been proposed. A comprehensive study on control has been given.
- Chapter 5 will discuss the conclusion and future work.

2. PROPOSED MVDC SYSTEM FOR MW LEVEL SPACECRAFT

2.1. Overview

2.1.1. Spacecraft Electric Propulsion

Traveling to Mars presents a multitude of challenges, including the distance from Earth and duration of the journey [59], radiation exposure [60], the complexity of entry, and landing, as well as the inhospitable Martian environment and propulsion. To ensure the viability and success of Mars missions, advances in electrical propulsion systems have become a key element due to their importance for overcoming distances, durations and harsh Martian conditions.

The improvement of electric propulsion (EP) systems has been drawn since 1960s when plasma sources capable of producing significant current were first created [61]. The first in-space demonstration of an EP took place in 1964 when an ion engine was used on the Space ERT-1 spacecraft and a pulsed plasma thruster (PPT) was used on the Soviet Zond-2 satellite. EP technology has advanced rapidly since then, leading to the development of new concepts. EP thrusters have been developed all over the world, many of which have operated successfully on satellites and space exploration probes. EP has started to reach its full potential in recent years, largely driven by the availability of power on space shuttles and high-powered electronic-based systems [62].

EP's operation is based on the law of momentum conservation. The thrust of the EP can be generated by expelling matter with high kinetic energy like chemical propulsion [63]-[64]. EP stands out due to its capability to attain high exhaust speeds by transferring a considerable amount of externally stored energy to the propellant. This characteristic leads to minimal propellant consumption during maneuvers, a significant advantage over chemical propulsion systems. EP's ability to operate for extended periods and its flexibility further underscore its benefits. Main

disadvantage lies in the current limitations of power supply, resulting in relatively low thrust levels. This limitation highlights the ongoing need for advancements in power generation, processing, and control technologies to enhance EP's performance and applicability in spacecrafts [64]-[65]. Authors in [66]-[67] discussed the EP technology covering the flight experience, operational characteristics, and spacecraft interactions. The plasma thrusters for space travel have been discussed in [68]-[69], while the authors in [70]-[71] discuss fundamentals of EP operation and compare different concepts.

Among the technologies being explored for MW-scale EP are Hall effect thrusters, ion thrusters, and magnetoplasmadynamic (MPD) thrusters. Each offers unique advantages in terms of efficiency, thrust, and operational lifespan, making them suitable for different aspects of interplanetary missions, from initial launch and transit to orbit insertion and station keeping. The authors in [72] compare different EP thrusters for small spacecraft, where they are classified into electrothermal, electrostatic and electromagnetic accelerations [73]-[80]. Authors in [73] concentrated on the preliminary design of a 50mN RESISTOJET propulsion system that operates at low pressure and uses a two-phase high-density propellant. The work in [74] focuses on developing a green propellant for CubeSats, addressing issues like space debris and propellant toxicity. A unique feature of the system proposed in [75] is its ability to utilize the unutilized pressurized gas from the liquid feed system once the liquid propellant is depleted, offering an advantage for cold gas propulsion. The authors in [76]-[77] introduced high-power EP systems, such as the inductive pulsed plasma thruster (IPPT) suitable for applications ranging from satellite maneuvering to deep space exploration. The IPPTs are further discussed in [78]-[79] highlighting their electrodeless design and the use of an inductive coil to accelerate propellant at high exhaust velocities. Authors in [79]-[80] presented a concept to control the ion flux distribution for a

magnetically enhanced thruster with an additional coil. It highlights that effective magnetic control is achieved when plasma density and spatial extent are having a correlation.

2.1.2. Energy Sources for Spacecrafts

In EP systems electrical energy is used to generate power for the electric thrusts in the spacecraft. Different electrical sources have been used, however, for MW-scale propulsion challenges exist in scaling conventional sources for high-power spacecrafts. Figure 11 depicts a paradigm of spacecraft power comparing different sources of power based on mission duration [9].

1. Primary batteries are suitable for short-duration missions or the initial stages of longer missions in space [81] such as small satellites orbiting the Earth or spacecrafts with power requirements of less than 10 kW. Small satellites including CubeSats [82] and other miniature spacecraft [83] often have limited space and weight capacity, making compact and lightweight primary batteries an attractive option for providing the necessary power for their operations. These satellites typically perform tasks such as Earth observation, scientific research, and communication relay for a limited period, ranging from a few days to a few years before their batteries are exhausted. For spacecraft with power needs of less than 10 kW, primary batteries can provide a simple and reliable power source for the initial stages of the mission. For example, they can be used to power the spacecraft's systems during launch and deployment, after which the spacecraft might switch to a more long-term power source like solar panels or a secondary (rechargeable) battery system [84].

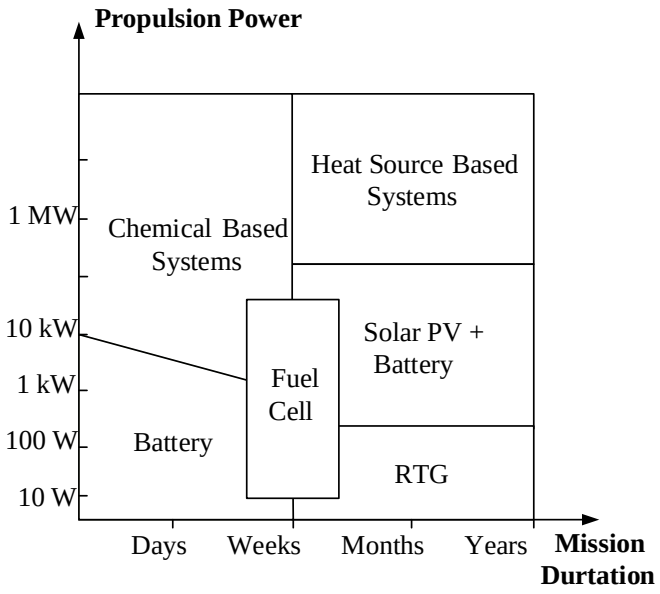

Figure 11. A paradigm of spacecraft propulsion power and source.

2. Fuel cells are a power source that may be used for missions that require more energy and longer durations than what primary batteries can provide [85]. Unlike batteries, which store chemical energy and convert it to electrical energy, fuel cells generate electricity through a chemical reaction between a fuel (usually hydrogen) and an oxidant (usually oxygen) with water and heat as byproducts. NASA's fuel cell usage to-date has consisted of Proton Exchange Membrane Fuel Cells (PEMFC) and Alkaline Fuel Cell (AFC) technology [86]. AFC were first used in space on the Gemini missions, but their most notable application was on the Apollo spacecraft. The Apollo Service Module was equipped with three fuel cells, each capable of producing 1.5 kW of power [87]. The Space Shuttle orbiters had fuel cell power plants that supplied electricity and water during missions [88]. While fuel cells have been a valuable asset in spacecraft missions, they are not without limitations. Challenges such as the storage of volatile fuels, the complexity of thermal management in space, and the weight and volume constraints of spacecraft systems must be addressed. Additionally, the initial cost and maintenance of fuel cell systems can be high.

3. Solar (PV) sources in combination with batteries offer viable solutions for long-range missions with powers of up to a few hundred kWs, as long as they have a decent distance from the Sun. These systems are common for satellites and low earth orbit (LEO) missions.
4. Radioisotope thermoelectric generators (RTGs) convert the heat released by the decay of radioactive materials into electricity. They are commonly used in deep space missions when solar power is not applicable. However, their power is limited, commonly below a few hundred watts. The authors in [89] designed a low-radiation, lightweight RTG for space exploration using a Monte Carlo model to evaluate alternative radioisotopes and proposing materials for housing and encapsulation. A historical review of RTGs and thermoelectric conversion is also presented for performance comparison in [89]. However, for a long-lived operation the Multi-Mission Radioisotope Thermoelectric Generator (MMRTG) power system is a better option due to its power and long lifespan of at least 14 years [90], albeit at powers of up to sub-kW. Authors in [91] analyzed the performance of the MMRTG engineering unit (EU) to improve confidence in power predictions for the first flight unit (F1). The EU's testing under simulated conditions similar to F1 on Mars showed a consistent degradation pattern indicating robust MMRTG performance predictions.
5. The only two sources suitable for MW-scale spacecrafts are chemical-based sources and heat source-based systems, i.e., nuclear power. While the chemical-based systems offer high-power they can only last for short missions leaving nuclear power as the only viable energy source for MW-scale long missions. The MW-scale sources are described in detail in the following section.

2.1.3. The Role of MW-Scale Propulsion in Interplanetary Travel

For missions that require MW-scale power, such as interplanetary crewed Mars missions, two sources of energy are viable, Figure 11: (i) Chemical-based sources for short to medium term missions, and (ii) heat source-based sources for short-, medium- and long-term missions, such as nuclear thermal propulsion (NTP) and nuclear electric propulsion (NEP) due to their high energy density and efficiency [92]. NTP uses a nuclear reactor to heat a propellant, providing higher specific impulse and shorter travel times compared to conventional chemical propulsion. NEP, on the other hand, uses a nuclear reactor to generate electricity, which powers electric propulsion systems like ion thrusters. This allows for very high specific impulse and long-duration deep space missions.

Figure 12 shows the mission path designed by NASA for a crewed large-spacecraft travel to Mars, which lasts approximately 650 days with 30 days stay on Mars. The mission is planned for a launch in 2027 with the planned arrival of Mars in April 2028. It takes 217 days for an outbound flight to Mars and 403 days on the return trip back to Earth. The mission has separate cargo and crewed vehicles with assembly orbit in LEO or cislunar space.

NASA has developed a propulsion concept for NEP/NTP for a spacecraft for Mars transit sized for four crews whose parameters are listed in Table 2 [93]. The work in [94] provides a technology maturation strategy by NASA's Space Nuclear Propulsion project to advance the readiness of critical technology elements for a high-power NEP. This strategy aims to mitigate risks associated with the development and future use of NEP by focusing on the demonstration of 1 MWe-class building blocks for major non-nuclear elements and critical reactor technologies. The plan emphasizes testing subsystems at relevant scales and environments to gain confidence in

their performance, wear mechanisms, and failure modes targeting a Technology Readiness Level (TRL) of 5 for each subsystem.

In [95] three different models have been proposed, (i) a detailed trajectory model to estimate the vehicle mass required for mission success as a function of NEP system, (ii) a power system mass model to estimate specific mass of NEP as a function of power and radiator mass assumptions and (iii) a power conversion system thermodynamic model to predict the radiator area required for a Brayton cycle power conversion system. Overall, the paper suggests that continued development and refinement of these models will provide deeper insights into the system-level effects of technology development choices for NEP power systems, aiding in the optimization of mission vehicle mass and architecture for crewed Mars missions. The authors in [96]-[97] proposed combination of NEP with chemical propulsion for Mars spacecraft propulsion. This hybrid propulsion demonstrates the potential to decrease the risk, complexity, and possibly the cost of crewed Mars missions compared to full NEP.

An outline of the current state of development in NEP and NTP can be found in [98]. Achieving the readiness of NEP systems for high-power missions, particularly for human Mars expeditions, hinges on a robust hardware testing strategy that mirrors the anticipated operational conditions. This approach ensures that the propulsion systems meet the stringent requirements for interplanetary travel including reliability, performance, and safety. Beyond technical feasibility, the evaluation of NEP/NTP systems for human Mars missions involves assessing their ability to reduce travel times, mitigate space radiation exposure, and provide adequate power for life support and scientific operations. This holistic approach is vital in determining the suitability of NEP systems for crewed missions to Mars.

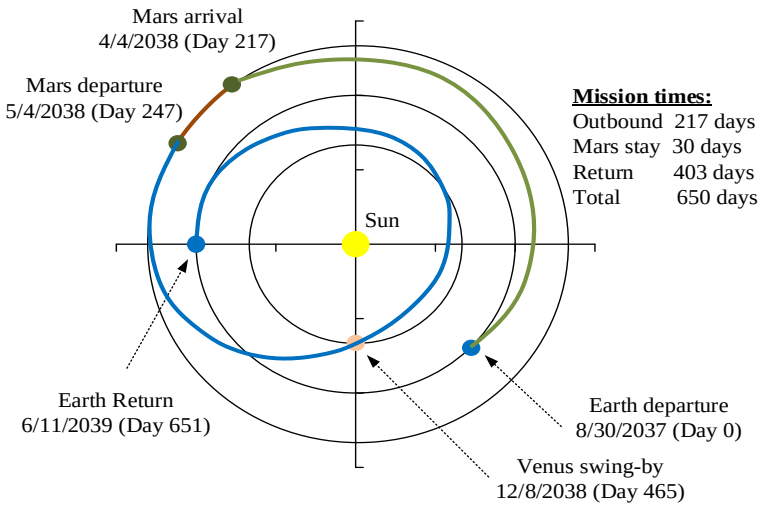

Figure 12. Opposition Class: Short-Stay Mission on Mars [93].

Table 2. Comparison of transport options on Mars with nuclear enabled, opposition class [93].

NEP	NTP
➢ specific impulse of at least 2000 (Isp) ➢ Specific mass below 20 kg/kWe ➢ Electrical power: 1 to 2 Mwe ➢ Reactor thermal power: 3 to 10 MWth ➢ Operational lifetime: 4 years for power generation, 1 to 2 years for thrust ➢ Voltage level of 1 kV, ➢ Frequency range of 2 kHz	➢ Nuclear thermal rockets with specific impulse of 900 (Isp) with up to 2500 lbf/engine ➢ Hydrogen propellant heated to at least 2500 K ➢ Reactor thermal power: ~500 MWth ➢ Operational lifetime: 4 h (intermittent operation: 6 to 8 restarts)

Authors in [99]-[100] have provided an overview of major elements of NEP, which is divided into five critical technology elements, Figure 13:

I. Nuclear reactor system (RXS) as the power source where the nuclear reactions provide the energy needed for the propulsion. The fuel of the reactor is Uranium. RXS generates heat as a result of nuclear fission, which will be converted to electrical power in the next stage

of propulsion. It should be noted that the NEP shield in Figure 13 serves to protect the rest of the spacecraft from radiation emitted by the reactor.

II. Power conversion system (PCS) that transforms nuclear heat into electrical power. The PCS's main components include a heat cycle that takes the heat from the reactor and processes it to a turbine that spins a generator. different heat cycles have been proposed for PSCs including Rankine/Hern, Thermo-acoustic, Brayton, Stirling [101]-[102], however, Brayton cycle has attracted more interest due to its high efficiency, long life, and scalability to high power [103]. The turbine in the PCS is designed to operate at temperatures above 1300 K [104], with a speed range of up to 75000 rpm for the turbine [102]. The turbine provides mechanical power rotating the generator whose output is electrical power, i.e. AC voltage and current. The authors in [105] conclude that a Brayton cycle combined with a high-speed turbine and a permanent magnet (PM) synchronous generator is a promising approach for PCS for the large spacecrafts. Key performance parameters for the PCS that are appropriate for human Mars mission have been mentioned in [106]-[107]. The summary of the finding mentioned the power level from 0.5 MW to 4 MW, a voltage level of 1 kV, and a frequency range of 2 kHz, which are included in Table 2.

III. PMAD that processes the generator's electrical power and may include components such as power electronics converters, control, and monitoring systems that manages the electrical power supplied to the electric thrusters and other spacecraft electrical power systems. NASA's PMAD requirement for NEP include [108]: Operating lifetime: 2 to 10 years; power level: 100 kW to 10 MW; and voltage level: 200 to 10,000 V. Note, the PMAD specifications need to match those of the electric generator output, which are ultimately defined based on the mission and spacecraft design.

IV. The electric propulsion subsystem (EPS) which includes the electric thruster, and its power processing unit, which is a power electronics converter that controls the voltage and current into the thruster. The thruster is chosen based on the specific impulse, efficiency, mission requirements and spacecraft design. Three major electric thrusters are Hall Effect thruster, Ion thruster, and MPD thruster [109]-[110].

V. The primary heat rejection system (PHRS), which is usually made of materials that are effective at absorbing radiation. The PHRS includes radiators that play a crucial role in the NEP's heat rejection process by dissipating excess thermal energy into space to maintain optimal operating temperatures for the spacecraft's components. There are seven critical technologies of radiator systems [105].

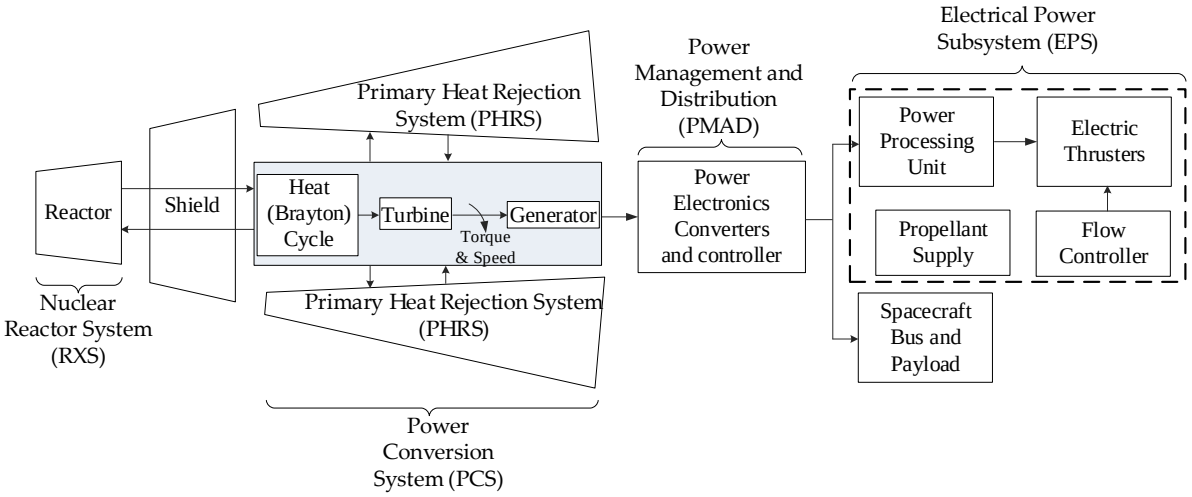

Figure 13. NEP main elements [102].

It should be noted that the utilization of NEP in the context of a spacecraft's mission, involves a multi-stage process that begins with the spacecraft's launch from Earth and transitions to the use of NEP once the spacecraft reaches LEO.

The spacecraft is launched from Earth using conventional chemical rocket thrusters. These thrusters provide the high thrust necessary to overcome Earth's gravitational pull and atmospheric

drag. Chemical rockets are preferred for this stage due to their ability to produce a large amount of thrust in a short time, allowing the spacecraft to reach LEO quickly.

Once in LEO, the spacecraft prepares to transition to NEP for the remainder of the mission. This often involves deploying the spacecraft from the launch vehicle or detaching parts of the spacecraft that were only necessary for the initial launch phase [106].

In the safety of LEO, where the risk of radioactive contamination to Earth's environment is mitigated, the NEP system is activated. The NEP provides a low thrust but high specific impulse, which means it is very fuel-efficient, producing a small amount of thrust over a long period. This is in contrast to chemical rockets which provide a high thrust over a short period.

Using NEP, the spacecraft begins the cruise phase of the mission. The propulsion system gradually increases the spacecraft's velocity over time. This gradual acceleration is suitable for interplanetary travel, as it conservatively uses the limited nuclear fuel supply and takes advantage of the NEP system's high efficiency.

As the spacecraft approaches Mars, the NEP system can be used to decelerate the spacecraft for orbit insertion. This phase of the mission would be carefully planned to ensure the spacecraft enters Mars' orbit with the correct speed and trajectory.

Once in Mars orbit, the spacecraft can commence its surface mission objectives. Should the mission design include a return trip to Earth, the NEP system would once again be employed to exit Mars' gravitational influence and propel the spacecraft back to Earth, using the same principles of gradual but efficient thrust.

It's worth noting that NEP systems are not used during the launch phase from Earth due to safety concerns. In the event of a launch failure, a nuclear reactor could pose a significant risk if it

were to explode or disintegrate in Earth's atmosphere. By initiating NEP use only once safely in space, the risk of radioactive contamination to the planet is significantly minimized [107].

2.2. Power Conversion Between Three Different Energy Sources

The need for power conversion in spacecraft arises from the necessity to efficiently utilize and manage the energy harvested from various sources and to supply it to the propulsion system and the loads in a form that is compatible with its operational requirements. Power conversion ensures that the electrical energy generated is transformed into the appropriate voltage and current levels required by the propulsion system and the loads, which is essential for maintaining the spacecraft's trajectory in space. The interplay between efficient energy management and the dynamic nature of power conversion underscores the complex challenges faced by spacecraft power systems. As the operating point continues to fluctuate due to the constant search of maximum power point tracking (MPPT) which the PV source can produce, the dynamic behavior of the used DC-DC converter will be disturbed at all times [42].

A PV panel under irradiation exhibits I-V characteristics with a unique point, MPPT, where the PV panel produces maximum output power. Author in [111] proposed a DC-DC converter at the panel level for the issue of power output reduction in solar PV panel strings due to mismatch between panels by partial shading. When mismatch occurs, either the panel-integrated diodes bypass the shaded panels, resulting in a loss of power, or the current of the entire string is reduced to match that of the shaded panels, leading to a further loss of power. The proposed work can generate power with 168% of power conversion efficiency than the conventional methods. While author in [112] discusses the design and implementation of an isolated high-frequency (HF) multiport DC-DC converter for PV interfacing systems. The converter uses an HF transformer with multiple input windings for each PV module and a single output winding connected to a DC

bus. A unique feature of this system is the use of a two-quadrant inverter topology for each input port, which prevents current from flowing back from the AC side to the DC side. In PV generation systems a DC-DC converter is required to connect the low volage PV and the high volage DC link MPPT control is vital to enable the full capacity of solar PV in DC-DC converter [113]-[114]. High tracking accuracy, stable transient response, and steady-state performance are key factors for evaluating MPPT techniques.

In [115]-[118] P&O algorithm which detects the MPP of the PV, studied. However, the output of the P&O algorithm has oscillation around the MPP. In [115] the speed controller is utilized in transient time by adapting scaling factor. To adjust the scaling factor, in [118], a flat scale factor is used. Current sensorless MPPT has been proposed in [119], where PV voltage is measured and cell temperature is estimated, so PV current can be measured from a proposed lookup table in [120], but this technique is plagued with complexity and reliability problems. Due to problems with ambient temperature estimation and model accuracy.

The method introduced in [121] eliminates the need for one current sensor by estimating the PV current using two measurable variables: the PV voltage and the output inductor current. While this approach is effective in tracking MPP, it necessitates careful attention to ensure the stability of the system. Multivariable control systems require finite-set model predictive control (FS-MPC) [122]. Model predictive control (MPC) based on MPPT has been studied in [123]-[124]. The MPC-based MPPT technique described in [83] efficiently tracks the maximum power output of PV modules under different environmental conditions. However, this method requires the use of three sensors: two for voltage and one for current. While the MPC-based MPPT technique provides efficient tracking of maximum power output, its reliance on multiple sensors adds complexity and cost to the system [125]. In contrast, the study of two aspects of MPP and P&O

for PV panels reveals an alternative approach. This approach involves a PV panel controller operating in current control mode, which allows for a rapid response to sudden changes in irradiation. By quickly adjusting the current reference to the controller, the system can adapt to changes in irradiation more effectively. The proposed method has demonstrated that the tracking speed can be increased by a factor of two, and oscillations can be reduced by 30%, offering a potentially more efficient and responsive solution for PV systems [126].

The integration of a BESS is essential for maintaining a stable and reliable energy supply. By providing a buffer during periods of low solar irradiance or system disturbances, the battery backup ensures a continuous power supply, enhancing the overall resilience and efficiency of the energy management system in spacecraft. Because of this solar panels' characteristic, spacecrafts use batteries as a backup energy source. The solar powered spacecraft produces more power than what the spacecraft needs since the power system needs to charge the batteries in time of eclipse [127]. To achieve this, advanced battery management must be incorporated into aircraft power management systems. Battery management system monitors and controls the storage and delivery of solar power drawn from solar cells. Battery modules are the main components of a battery management system. Compared to alternative battery technologies, Li-ion batteries offer high energy density, flexible and light-weight design, no memory effects, and a long lifespan [128]. These features of Li-ion batteries make them highly suitable for electric vehicles (EVs) and aerospace applications [129]-[131].

Primary battery management measures the observable quantities like voltage, current, temperature and state estimation for battery performance computations [132]. The bidirectional power flow for charge/discharge of the BESS requires a bidirectional isolated DC-DC converter. Authors in [133]-[135] provided a general literature review of DC-DC converters connected to the

Li-Ion BESS. Due to nature of space application scenarios including periodic charge and discharge, nearly constant discharge current, low electric current rate, and fixed depth of discharge, which bring challenges to battery pack state-of-health estimation. Author in [133] introduced an empirical model to improve the accuracy of discharge process under constant current. However, the proposed method is only valid under special operating conditions. In [134] a dynamic model for the battery charging process is proposed. The battery is charged using a non-inverting synchronous buck-boost DC-DC power converter. According to the supply voltage conditions of PV panels the proposed design estimated the battery dynamics.

The authors of [135]-[137] studied the current-source full bridge converter topology that has a dc-link inductor connected to the low-voltage bridge. It can minimize ripple current at the 12-V battery side of a fuel-cell EV application. The converter topology is also considered for a 100-kW, wide operating voltage range application in [138]. The converter, however, suffers from high device voltage stress and needs an active clamp consisting of an active switch and a capacitor rated at full load for voltage clamping and to absorb the difference between the dc-link inductor current and transformer leakage-inductor current.

The voltage-source full-bridge bidirectional isolated DC-DC converter is studied for high-power automotive applications [139]-[141]. High-power transfer capability in the converter can be achieved using simple phase-shift-modulation techniques. However, the modulation techniques require complex computation. Authors in [142] studied a buck converter to charge the BESS for increasing the reliability of it. In this energy management system, it is considered that when the production is more than demand, the extra energy will charge the battery and no energy is transferred from the grid to the system. However, demand and battery charging will be compensated by the grid when there is a shortage of input power to supply electricity. While

authors in [143] investigated a problem of regulating output voltage for a battery powered boost converter when load is uncertain or changes in certain ranges. The battery with two capacitors is modeled with a second order circuit. The optimized state feedback and the integrator feedback can be regulated in the presence of uncertain load and battery voltage.

Figure 14 shows the medium MVDC microgrid system proposed for the Mars mission spacecraft. The core objective of the MVDC microgrid is to optimize the power and propulsion system by efficiently managing multiple power sources, including a NEP system, PV panels, and BESS. The solar panel voltage varies from 120-385V and connects to the DC bus using a DC-DC converter. Similarly, to convert the voltage of the BESS and charge/discharge the energy storage, a bidirectional DC-DC converter is employed, allowing the voltage to be increased from 320 V to 1000 V. An Adaptive Solar Controller for Maintaining MPPT under Variable Temperature and Solar Intensity has been indicated. Battery Charge/Discharge Rate is achieved with BESS controller. PM generator has been connected to NEP for power generation from Thermal Energy. NEP uses a nuclear reactor and turbine to drive an PM to generate electrical power. The 3-phase rectifier has been introduced to maintain the voltage and power that has been generated from heat source. Most of the power that has been produced from the NEP would be used for the thrust of the spacecraft. On the thruster side, an isolated DC-DC converter with controlled current output ensures optimal interfacing with the propulsion system.

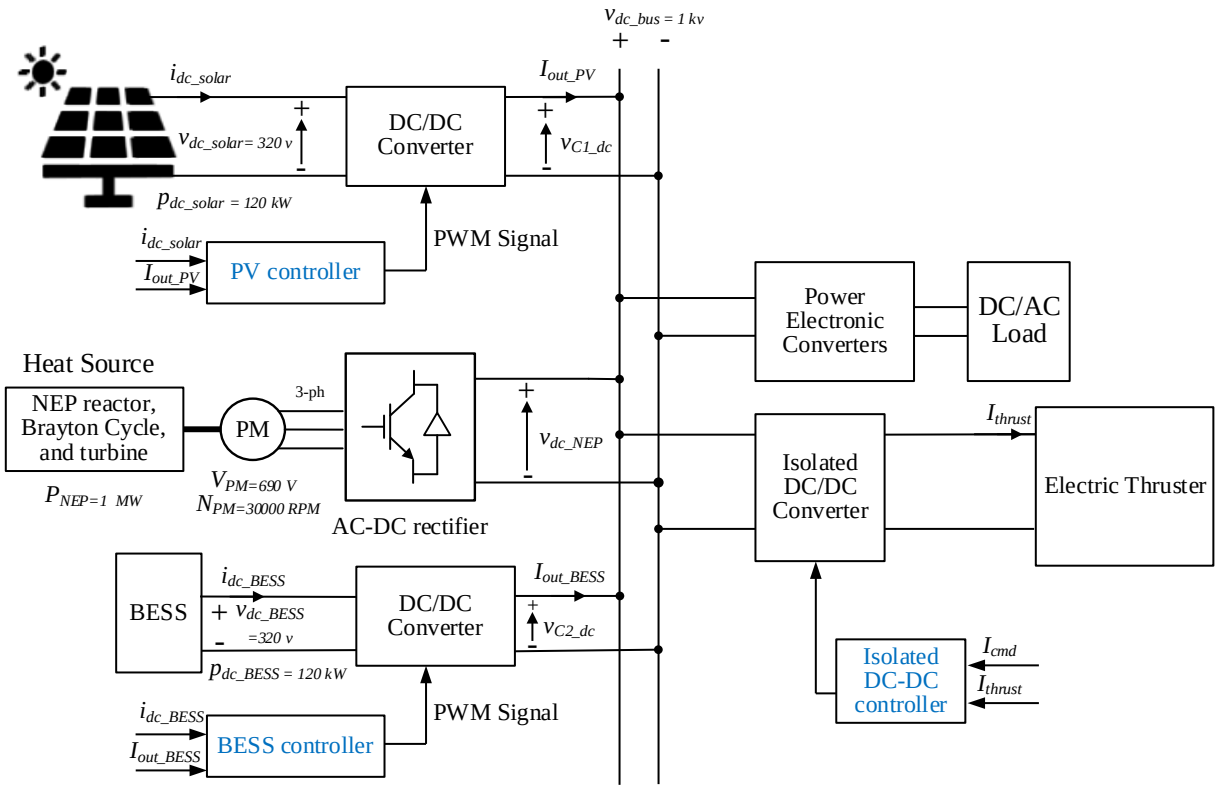

Figure 14. MVDC microgrid for Mars mission.

3. BOOST CONVERTER CONTROL FOR SOLAR AND BESS

3.1. Converter Topologies

As discussed previously, the NEP is connected to the MVDC grid through a 3-phase rectifier. The NEP rectifier is regulating the bus voltage, i.e., regulating the 1000 V MVDC grid voltage. Given the limitations provided in section 2.1 regarding the solar PV systems, in terms of scalability and dependency on solar irradiance, it becomes imperative to explore efficient energy conversion and management solutions. PV power varies with temperature, irradiance and load characteristics [144]-[145] and it is directly proportional to irradiance and inversely proportional to temperature. Thus, the role of power converters is a critical component in optimizing the performance of solar PV systems [146]. For effective use of PV panels, DC-DC converters are included in PV implementations [147]. Switching devices like MOSFETs and IGBTs are commonly used in converters for solar energy applications. These high voltage converter switches typically operate at a switching frequency greater than 10 kHz and can handle voltages up to 1.2 kV. However, in high voltage converters, the switching frequency is usually limited to around 1 kHz due to increased switching losses.

Recent advancements in the manufacturing of switching devices have helped to overcome this limitation, allowing for higher switching frequencies. The author in [148] presented a high-power boost converter using SiC JFET as switching device that can operate up to 300 kHz. By using a MOSFET with a low drain source on resistance, the conduction loss can be largely reduced [149]. The cost, efficiency, energy flow and ability to maintain the output irrespective of any input variations are a primary criterion for choosing DCDC converters in PV installations. The influence of voltage ripple on the output side of PV module should be minimum as possible [150]. The hardware complexity of the converter consists of the filter size and the gate drive circuit. The

single-ended primary-inductance converter (SEPIC) has a high output voltage ripple at output side compared to the other converters. Table 3 indicated a comprehensive analysis of cost, efficiency, hardware complexity in boost, buck, buck-boost, SEPIC and flyback converters. The efficiency of a converter can be calculated by,

$$\eta_{converter} = \frac{V_{out} \cdot I_{out}}{v \cdot I_{pv}} = \frac{v \cdot I_{pv} - P_{losses}}{v \cdot I_{pv}} \quad (2)$$

where V_{out} is the voltage of the converter at the output side, I_{out} is the output current of the converter, v is the voltage at the output of the panel, I_{pv} is the current at the output of the panel and P_{losses} is the losses of the converter.

Table 3. Comparison of various converters [151]-[156].

Characteristics	**Buck**	**Boost**	**Buck boost**	**SEPIC**	**Flyback**
Efficiency	High	High	Medium	Medium	Medium
Cost	Medium	Low	Low	Medium	Medium
Hardware complexity	Medium	Medium	Medium	High	High
Energy transferring elements	Inductor	Inductor	Inductor	Inductor and capacitor	Transformer

Several studies have reviewed the topologies for converters in renewable energy systems. Although SEPIC, Cuk and buck-boost converters have high ripple in the load current, they have flexibility over output voltage. In comparison to these topologies, buck topology shows high current ripple [156]. The buck converters are rarely used as DC-DC converters because the PV arrays output voltage is always less than the grid voltage. Since the array Current output from the converter has current pulses, to smooth the array's current, a capacitor is required. Of all the mentioned converters in Table 3, boost converter is the most suitable converter for PV modules [157]-[158]. Similarly, in the development of BESS, the efficiency of the converter in facilitating bidirectional energy flow is the most important factor. Among all the mentioned converters in

Table 3, boost converter has the most efficiency, therefore, it has been chosen for the design of this spacecraft [159].

For the PV, as shown in Figure 15, the current remains roughly constant as the voltage increases, up to the MPPT point. Beyond this point, the current plummets with further increases in voltage. For our DC-DC converter, employing a current control mode is the most appropriate approach to address this phenomenon, as it allows for effective management of the current drop after the MPPT point. This ensures improved dynamic performance and stability of the system.

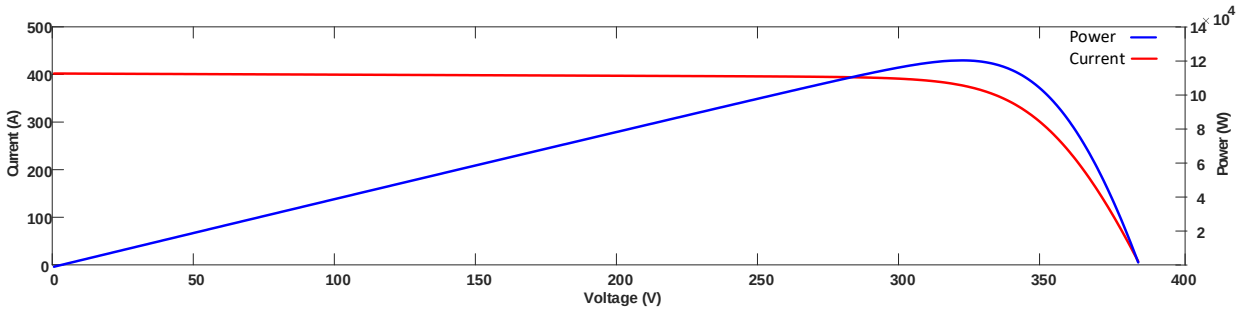

Figure 15. Solar panel characteristics.

3.2. Review of Boost Converter

High voltage step-up is necessary in several applications such as spacecraft power systems, especially considering that DC-DC converters must be supplied by high DC voltages. The conventional boost converter is able to step the input voltage up to three or four times because the high output voltage demands high duty cycle values, therefore this is one of the most popular topologies [160]-[163]. This converter leads the switch to remain on for long time intervals [164]. Figure 16 shows the schematic of boost converter, where L is the input inductor, C is the output capacitor, I_L is the inductor current, V_{in} is the input voltage, V_{out} is the output voltage, the UDE controller is the proposed control algorithm that will be introduced in the following chapter. Then the state-space model of the converter can be written as the following equations [165],

$$\begin{cases} L\dfrac{dI_L}{dt} = V_{in}(0\sim DT_s) \\ L\dfrac{dI_L}{dt} = V_{in} - V_{out}(DT_s\sim T_s) \end{cases} \tag{3}$$

$$\begin{cases} C\dfrac{dV_{out}}{dt} = -I_{Load}(0\sim DT_s) \\ C\dfrac{dV_{out}}{dt} = I_L - I_{Load}(DT_s\sim T_s) \end{cases} \tag{4}$$

where D is the duty cycle of the boost converter gate signal. Combining (3) and (4), the dynamic model of the boost converter can be written as [166],

$$\begin{cases} L\dfrac{dI_L}{dt} = V_{in} - (1-D)V_{out} \\ C\dfrac{dV_{out}}{dt} = (1-D)I_L - I_{Load} \end{cases} \tag{5}$$

Equation (5) shows that the converter is in non-minimum phase and nonlinear, which increases the design difficulty.

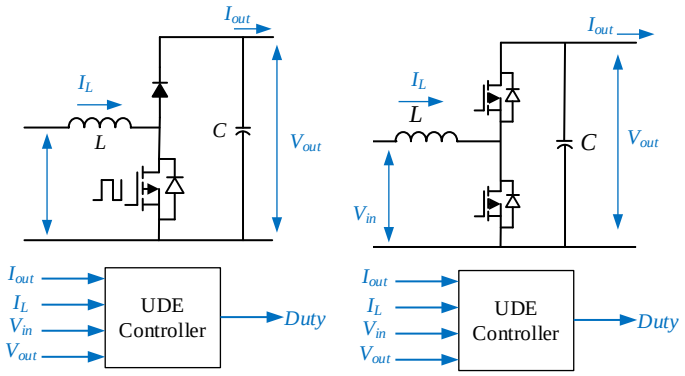

Figure 16. Schematic of the UDE-controlled boost converter (a) Unidirectional for PV, (b) Bidirectional for BESS.

3.3. Review of UDE Algorithm

Performance of practical control systems is worsened by disturbances and uncertainties. External disturbances to the environment, unmodelled dynamic and parameter disturbances, which have led to deterioration [167]. For the purpose of ensuring satisfactory

performance and stability, uncertainty and disturbances rejection is therefore one of the most important objectives for industrial control system design [168]. In many cases, external disturbance and uncertainty cannot be measured directly. The idea of disturbance observer-based control is to estimate the disturbance from measurable variables and compensate for the influence of the disturbance. During recent decades, different disturbance observer-based techniques have been widely studied and utilized in industrial applications [169]-[172]. One approach that has become popular is the use of uncertainty and disturbance estimator (UDE)-based control, which seeks to provide an alternative method for managing time delays by estimating a combined impact of disturbance and uncertainty. This aims to address the control of time delays through estimation of their combined effect alongside disturbances and uncertainties. UDE performance is based on the assumption that effective filtering can closely approximate any continuous physical signal [173]. UDE-assisted sliding mode controllers were studied in [174]-[176] and UDE-based robust input–output linearization was revealed in [177]-[178].

A linear system with uncertainty and disturbance can be described as,

$$\dot{x}(t) = (A + \Delta A)x(t) + Bu(t) + f(t) \tag{6}$$

Where $u(t)$ is the input for the system and $x(t)$ is the state of the system. A and B are defined as state matrixes, ΔA represents the unknown system matrix, and $f(t)$ is the external disturbances. $u_d(t)=\Delta Ax(t)+f(t)$ is the impact of the disturbances and uncertainty [179].

The aim of UDE is to remove u_d and drive the system state $x(t)$ to follow $x_m(t)$ as a reference. $x_m(t)$ can be defined as,

$$\dot{x_m}(t) = A_m x_m(t) + B_m r(t) \tag{7}$$

Where A_m and B_m are matrixes of the reference system that the actual system should track. Reference signal for this system is $r(t)$. For achieving the high accuracy tracking of the reference

system $x_m(t)$, the tracking error is defined as $e(t)=x_m(t)-x(t)$, the dynamics of the error can be defined as follow:

$$\dot{e}(t) = A_m e(t) + Ke(t) \tag{8}$$

Where K is the state-feedback gain and A_m+K should be Hurwitz. Based on (6)-(8), the control law can be designed as,

$$u(t) = B^{+}[A_m x(t) - Ax(t) + B_m r(t) - Ke(t) - u_d(t)] \tag{9}$$

Uncertainty and disturbances $u_d(t)$ is usually unknown for most of the applications. In order to realize the control law in (9), here, an estimated uncertainty and disturbances $u_{de}(t)$ proposed. The estimate $u_{de}(t)$ can be written as,

$$\begin{aligned} u_{de}(t) &= g_f(t) * u_d(t) \\ &= \mathcal{L}^{-1}\{G_f(s)[sx(s) - Ax(s) - Bu(s)]\} \end{aligned} \tag{10}$$

Where G_f is the uncertainty and disturbance filter. Within the bandwidth of G_f, the estimate $u_{de}(t)$ is almost the same as the actual disturbance $u_d(t)$. Thus, the control law in can be written as,

$$u(t) = B^{+}[A_m x(t) - Ax(t) + B_m r(t) - Ke(t) - u_{de}(t)] \tag{11}$$

3.4. UDE Current Control for Boost Converter MVDC

In the proposed system, the boost converters for Solar panel and BESS are in the current control mode. As mentioned earlier, the boost converter model is given in (5) in non-minimal phase and nonlinear. To simplify the design's complexity, a virtual control variables m can be introduced as follows,

$$m = 1 - D \tag{12}$$

then the boost converter model can be rewritten as,

$$\begin{cases} \dfrac{dI_L}{dt} = \dfrac{V_{in} - mV_{out}}{L} \\ I_{out} = mI_L \end{cases} \tag{13}$$

It should be noticed that the voltage dynamics of the boost converter are ignored here since the boost converter is working in the current control mode, i.e., the voltage is not controlled by the boost converter. Moreover, as (13) shows, the boost converter model is a nonlinear and nonminimal phase system. It should be noted that large-signal analysis is not pursued in this context due to its inherent complexity and nonlinearity, which makes controller design and system analysis significantly more challenging without providing additional benefits for typical operating conditions. In order to simplify the controller design, here the small signal model of the Boost converter is derived as follows:

$$I_{(out,0)} + \Delta I_{out} = (m_0 + \Delta m)(I_{L0} + \Delta I_L) \tag{14}$$

where $I_{out,0}=m_0 I_{L0}$ is the steady-state output current of the boost converter, m_0 and I_{L0} are the steady-state operation points, ΔI_{out}, Δm, and ΔI_L are the small signal items of I_{out}, m, and I_L respectively. Ignoring the high order term, the small signal model of the boost converter can be simplified as,

$$\Delta I_{out} = I_{L0}\Delta m + \Delta I_L m_0 \tag{15}$$

In the steady-state of the boost converter, we have and, based on (13) and (15), the small signal transfer function of the boost converter can be written as [180],

$$\frac{\Delta I_{out}(s)}{\Delta m(s)} = \frac{s\frac{V_{out}}{V_{in}} L I_{out,0} - V_{in}}{sL} \tag{16}$$

without losing generality, assuming $I_{out,0}=0$, and the linearized boost converter model can be written as,

$$\frac{dI_{out}}{dt} = \frac{-V_{in}}{L} m + f \tag{17}$$

where f is the system disturbance. In order to achieve the current tracking, here a reference system is defined as follows,

$$\frac{dI_m}{dt} = -\alpha I_m + \alpha I_{cmd} \tag{18}$$

where I_m is the reference current that I_{out} should track, I_{cmd} is the command current, and α is the desired bandwidth of the current tracking loop. The current tracking error can be defined as $e=I_m-I_{out}$ and it satisfies (15),

$$\frac{de}{dt} = -\alpha e - ke \tag{19}$$

where k is the proportional gain that can speed up the error convergence. Then the tracking error can be rewritten as,

$$\begin{aligned} \frac{dI_m}{dt} - \frac{dI_{out}}{dt} &= -\alpha I_m + \alpha I_{cmd} + \frac{V_{in}}{L} m - f \\ &= -\alpha e - ke \end{aligned} \tag{20}$$

Based on (20), the control law m should satisfy,

$$m = \frac{L}{V_{in}} (\alpha I_m - \alpha I_{cmd} - \alpha e - ke + f) \tag{21}$$

in (21), f is unknown disturbance, which can be written as,

$$f = \frac{dI_{out}}{dt} + \frac{V_{in}}{L} m \tag{22}$$

Based on the UDE law, the disturbance could be estimated as follows,

$$f_{est} = \left(\frac{dI_{out}}{dt} + \frac{V_{in}}{L} m\right) * G_f \tag{23}$$

Thus, the UDE-based current controller for the boost converter can be written as,

$$m = \frac{L}{V_{in}} (I_m - I_{cmd} - \alpha e - ke + f_{est}) \tag{24}$$

3.5. Simulation Studies

In order to validate the effectiveness of the proposed UDE control algorithms for the current mode boost converters, simulation studies have been conducted. The controllers used in simulations follow the design given in Section 3.4 respectively. Figure 17 shows the control

performance of the boost converter under the proposed control when the state-feedback control is enabled, and the disturbance estimation filter is set as 0, i.e., G_f=0. As it is indicated in the figure the state-feedback control can provide satisfactory dynamic voltage tracking performance when the disturbance estimation filter is not enabled. However, the state-feedback control cannot effectively reject the system uncertainty and disturbance, and thus, the voltage tracking steady-state error E_{ss} is not zero, which is about 38 A.

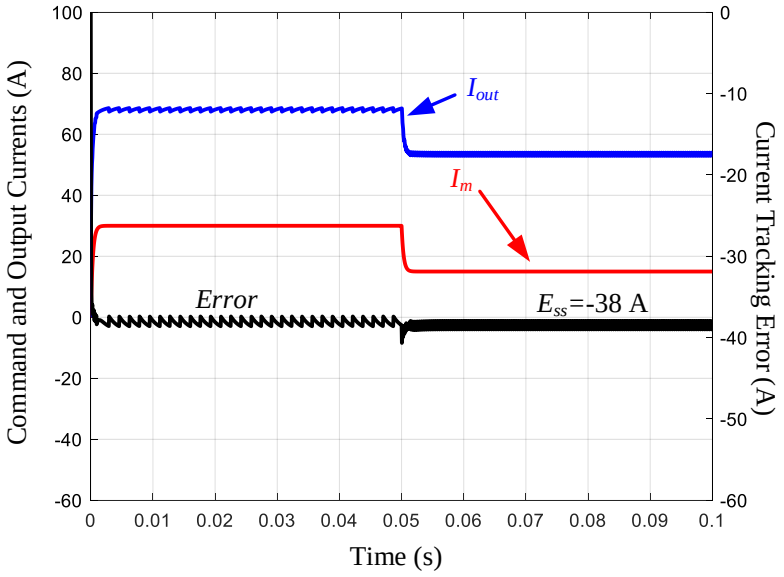

Figure 17. Current mode boost converter tracking performance under the UDE controller while the reference system bandwidth is 200 Hz, G_f = 0.

Figure 18 demonstrates the precision of the control systems in the condition when both the state-feedback control and disturbance estimator filter for boost UDE controller are enabled while the bandwidth of G_f is 200 Hz. This suggests that the proposed disturbance and uncertainty estimation filter G_f provides a satisfactory disturbance estimate and eliminates the current tracking steady-state error. The current is maintained withing a range of 0.67 % around the commanded current under load changes. The control system consistently meets the reference current without persistent deviation. The zero steady-state error indicates the ability of the controller to maintain

accuracy and stability in the long-term. In practice, the circuit parameters always have tolerances. A robust controller should be able to maintain the system stability and track the desired performance under these permutations. Under a condition when the circuit parameters have ±20% error while the bandwidth of G_f is 200 Hz, it can be seen from Figure 19 that the dynamic voltage tracking can still estimate the disturbance effectively and achieve the precise regulation. It can be seen that the parameter tolerance results in higher transient tracking error. However, the proposed control scheme is still able to eliminate the steady-state tracking error.

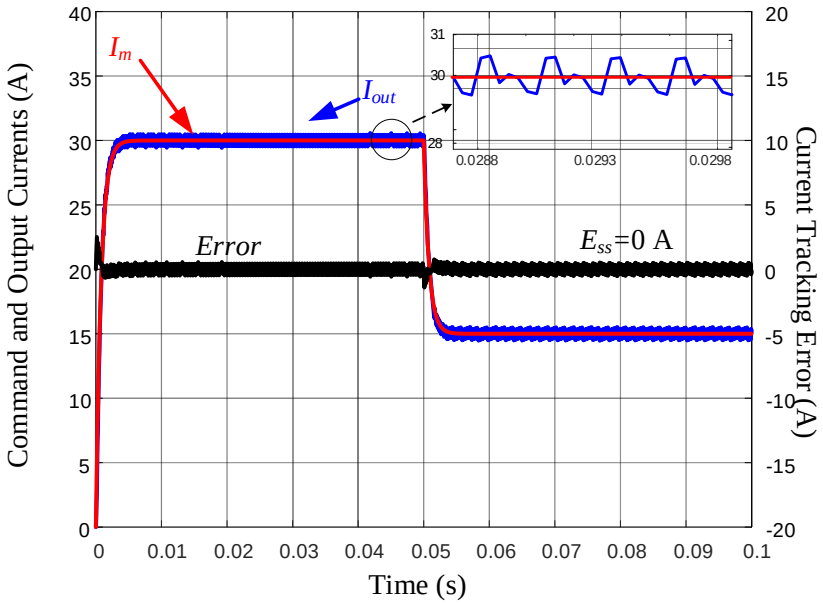

Figure 18. Current mode boost converter tracking performance under the UDE controller while the reference system bandwidth is 200 Hz and G_f = 200 Hz.

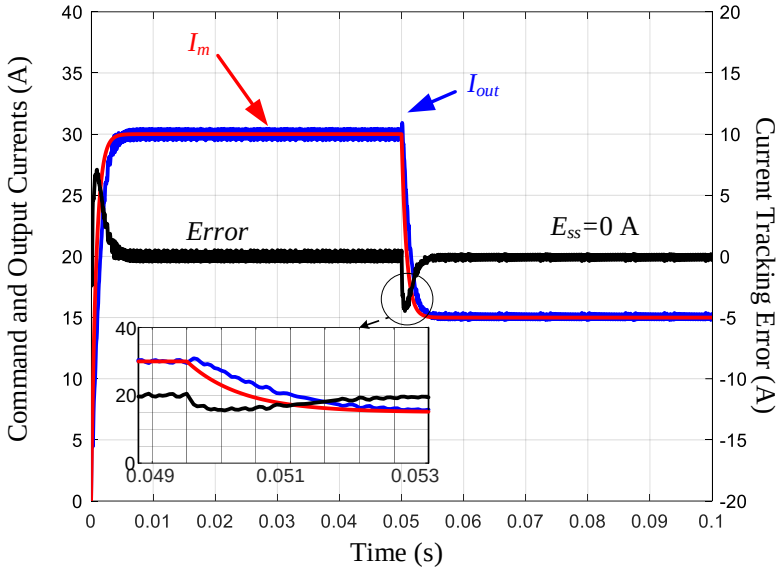

Figure 19. Current mode boost converter tracking performance under the UDE controller while the reference system bandwidth is 200 Hz and G_f is 200 Hz when the circuit parameters have ±20% error.

The proposed scheme is capable of actively estimating and compensating for system uncertainties and disturbances that are occurring with the boost converters, thereby enhancing the control performance and robustness of the system. Simulation studies have verified the effectiveness of the proposed schemes.

4. ISOLATED DC-DC CONVERTER CONTROL FOR PROPULSION SYSTEM

4.1. SAB and DAB Overview

Recently due to the high performance of isolated DC-DC converters, they are becoming more popular. Their main features include galvanic isolation, compact structure and high efficiency [181]-[184]. The most common converters are single active bridge (SAB) and dual active bridge (DAB). Resonant DC-DC converters like capacitor-inductor-inductor-capacitor (CLLC), inductor-inductor-capacitor (LLC) and inductor-capacitor (LC) are also commonly used due to their soft switching and better efficiency feature [185]-[186]. Figure 20 shows the general schematic of an isolated DC-DC converter. Bridge 1 is an active type and is used in all the types of DC-DC converters. While bridge 2 can be different types; for the DAB converters, it is of the active type and the bridge sides consists of controlled switches. However, for SAB, it is a passive type and bridge sides are composed of diodes. In Figure 20 includes, beside the bridges: (i) the capacitor (C_0), which filters the output voltage V_0, (ii) the inductor (L), which is the total leakage inductance of the isolation transformer, and (iii) the resistor (R), which describes the load.

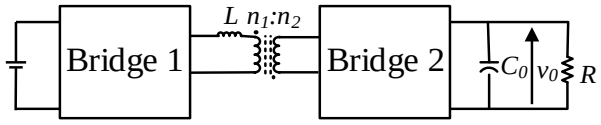

Figure 20. General structure of an isolated DC-DC converter.

For applications where unidirectional power transfer and lower power density is required, SAB could be suitable. SAB converter constitutes the inductor at the output. This converter has a unity voltage conversion ratio, as the inductor is bulky, it can operate in continuous current mode. The inductor and capacitor of the diode rectifier can generate a surge voltage; therefore, high voltage diodes must be used as the diode rectifier [187]. However, authors in [188]-[189] have suppressed the voltage surge by using an auxiliary circuit. By moving the inductor to the primary

side of the converter, inductance can be reduced by a factor of the square of the transformer turn-ratio.

Bridge 2 of the SAB only consists of diodes; therefore, it is the simplest converter among the isolated unidirectional converters. This bridge configuration decreases the cost and volume of DC-DC converter, and it can be used in a series connection to obtain a DC-DC converter with a medium-voltage rating. Authors in [190]-[192] did a comprehensive review of SAB converters with focus on half-bridge (HB) or full-bridge (FB) input. Author in [191] studied the dynamics and basic working principle of an HB SAB converter. While author in [193] analyzed the switching losses of the transistors of an FB SAB converter by implementing a dual-current phase control. Authors in [194] proposed a partial-resonant FB SAB converter in order to reduce the transistor conduction losses. The behavior of FB SAB converter with a voltage doubler by the influence of transformer turns ratio and leakage inductance has been studied in [195], where two capacitors have been replaced by one leg of the bridge 2 diode rectifiers. The design criteria and soft-switching capabilities of an FB SAB converters are compared to those of the DAB converters respectively in, [196]-[198].

As shown in Figure 21, SAB converter consists of two bridges coupled through a transformer. The primary-side bridge is an active type of bridge that is powered by the DC voltage V_{in}. It functions as an inverter and generates the AC high-frequency voltage v_1 at its output. Transistors can be MOSFET or IGBT for medium-high-power applications. The secondary-side bridge of the SAB converter is a passive bridge that is powered by voltage v_2 at the isolation transformer's secondary. The secondary bridge functions as a rectifier and the output voltage of the SAB converter V_{out}.

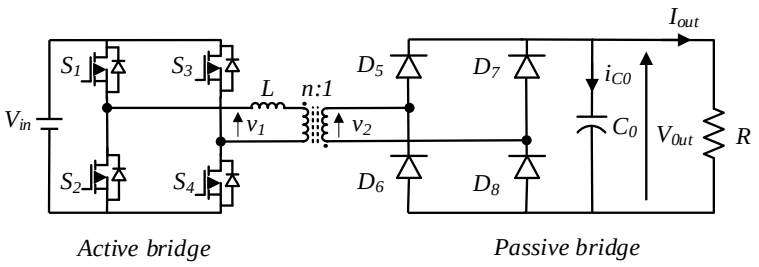

Figure 21. SAB converter schematic.

SAB converter can be operated in the continuous conduction mode (CCM). Figure 22 indicates the waveforms of voltages (v_1 and v_2) and output current (I_{out}), as a function of the angular quantity θ. The phase-shift angle of the two transistors on the same side ranges from $0<\alpha<\pi$. By analyzing the waveforms, odd symmetrical property with respect to π can be noticed.

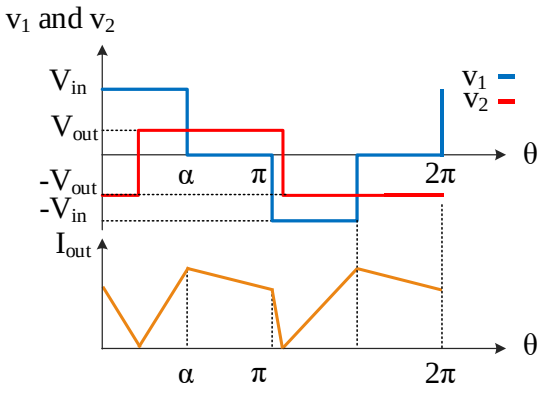

Figure 22. Voltages and currents waveforms of the SAB converter operating in CCM.

Among other isolated DC-DC converters, the Dual-Active Bridge (DAB) has gained a numerous attention recently, due to the improvement of new power devices and magnetic materials (especially the development of gallium-nitride (GaN) and silicon carbide (SiC) based power devices and nanocrystalline soft magnetic). This improvement reduced the bulkiness and heaviness of line–frequency (LF) transformers from PCSs [199]-[201]. PCSs utilize LF transformers to achieve galvanic isolation and voltage matching.

Nowadays, the utilization of HF transformers in place of traditional LF transformers is considered. High-frequency-link (HFL) PCSs based on HF transformers can attenuate the voltage and current waveform distortion which is made by the core saturation of LF transformers. HF-PCS noise is reduced compared to LF-PCS [198]. In numerous studies of HF-PCSs, isolated bidirectional DC-DC converters (IBDCs) are mainly considered in the power electronics circuit. The simplest IBDC topology is a dual-switch structure, such as: dual-flyback IBDC, dual-Cuk IBDC, and Zeta-Sepic IBDC [199]-[202]. The model of six-switch topology is half-full-bridge IBDC [203]. Eight-switch topology is mainly dual-active-bridge IBDC (DAB-IBDC) [204]-[206].

When the rated voltage and current of switches are the same, the transmission power of IBDC is proportional to the number of switches. For instance, four-switch IBDC has double switches compared to two-switch IBDC, but half of the eight-switch IBDC. Therefore, the DAB–IBDC has the biggest power capacity among others. From a filtering perspective, the output pulsation frequency for a forward converter is equal to the switching frequency, while for push-pull, half-bridge, and full-bridge converters, it is twice the switching frequency. Therefore, for the same output voltage, the filter required for a DAB-IBDC converter is also smaller. In fact, DAB converters were proposed in the early 1990s [207]-[209].

One of the main features of the DAB is the ease of soft-switching, bidirectional power transfer capability, and symmetric structure, etc. Comprehensive analyses of the design, operation and control of DAB in steady state were investigated in [204], [206]. In [210], boundary control scheme has been introduced while utilizing the natural switching surface. The short-time-scale transient processes with phase shift control has been studied in [211]. In [212], the design and performance of a 6 kW DAB converter to charge a Li-Ion BESS has been analyzed. The maximum

efficiency of the DC-DC converter is measured to be 96% and an analysis of the effect of unavoidable dc-bias current on the magnetic-flux saturations of the transformer has been studied.

As depicted in Figure 23, the basic design of a DAB converter includes two full-bridge converters, power MOSFETs labeled S_1 through S_8, a transformer's leakage L, which may also incorporate an additional external inductor, a high frequency (HF) transformer with a turns ratio denoted by n, an input voltage (V_{in}) an output of C, RL, and the output voltage (V_{out}) and current (I_{out}) [213]-[214]. The HF transformer provides the required galvanic isolation and voltage matching between two voltage levels. The auxiliary inductor is recognized as an instantaneous energy storage device.

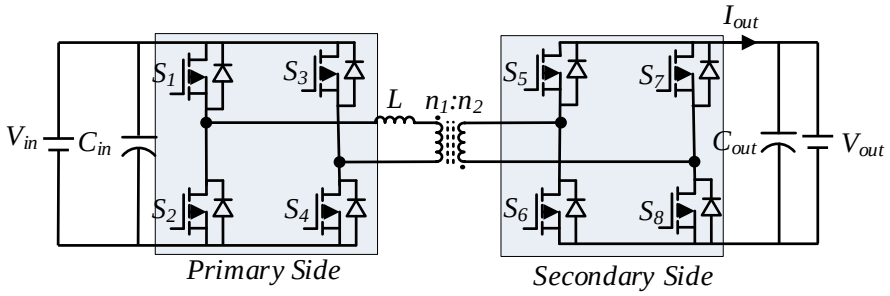

Figure 23. DAB converter schematic.

Figure 24 indicates the power transmission control in traditional ac power systems. By adjusting the magnitude and direction of the inductor current i_L, the phase shift between ac output square wave voltage v_{h1} and v_{h2} of primary and secondary side bridge can be achieved. Similar to the traditional systems, the same approach can be done for DAB converters. The difference is that the voltages in both sides of the inductor in traditional ac power system are line-frequency sinusoidal waves and in DAB-IBDC are high-frequency square waves. The transmission power of the traditional ac power system and of DAB can be calculated as,

$$\begin{cases} P_{sin} = \dfrac{V_{rms1}V_{rms2}}{2\pi f_s L} sin\theta \\ P_{square} = \dfrac{nV_1V_2}{2\pi^2 f_s L}\theta(\pi - \theta) \end{cases} \quad (25)$$

Where V_{rms1} and V_{rms2} are the root mean square (RMS) of sinusoidal waves and θ is the phase shift between ac voltages. The power density and modularity improve significantly because of HF power transmission. Therefore, DAB is the main core of HFL-PCSs.

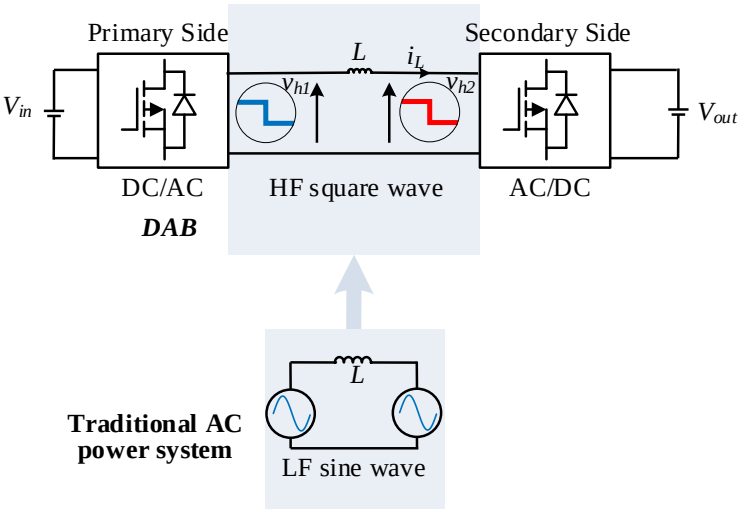

Figure 24. Traditional AC power system vs. DAB.

4.2. SAB Converter Control for Propulsion System

In the proposed MV Figure 14, a SAB DC-DC is one of the options that can be used as a power processing unit for the electric thruster, which can offer unidirectional power flow and low cost. Figure 25 shows the six equivalent circuit that characterize the converter in the continuous conduction mode (CCM) mode of operation. The inductor current (i_L) can be measured in all cases by applying Faraday's law.

- Cycle (t_0, t_1) has shown in Figure 25(a), where the semiconductor conducting the current are DS_1, DS_4, D_6 and D_7. Then i_L would be:

$$i_L = \frac{1}{L}\left(V_{in} + \frac{V_{out}}{n}\right)(t - t_0) + i_{L0} \tag{26}$$

Where i_{L0} is the inductor current at the start of this cycle and *DS* is the diode of primary side switches. When i_L reaches zero at t_1 this cycle ends.

- Cycle (t_1, t_2) has shown in Figure 25(b), where the semiconductors conducting the currents are S_1, S_4, D_5, and D_8. Then i_L would be:

$$i_L = \frac{1}{L}\left(V_{in} - \frac{V_{out}}{n}\right)(t - t_1) \tag{27}$$

- Cycle (t_2, t_3) has shown in Figure 25(c), where the semiconductors conducting the currents are DS_2, S_4, D_5, and D_8. Then i_L would be:

$$i_L = -\frac{1}{L}\left(\frac{V_{out}}{n}\right)(t - t_2) + i_{L2} \tag{28}$$

- Cycle (t_3, t_4) has shown in Figure 25(d), where the semiconductors conducting the currents are DS_2, DS_3, D_5, and D_8. Then i_L would be:

$$i_L = \frac{1}{L}\left(V_{in} + \frac{V_{out}}{n}\right)(t - t_3) + i_{L3} \tag{29}$$

- Cycle (t_4, t_5) has shown in Figure 25(e), where the semiconductors conducting the currents are S_2, S_3, D_6, and D_7. Then i_L would be:

$$i_L = \frac{1}{L}\left(V_{in} + \frac{V_{out}}{n}\right)(t - t_4) \tag{30}$$

- Cycle (t_5, t_6) has shown in Figure 25(f), where the semiconductors conducting the currents are DS_1, S_3, D_6, and D_7. Then i_L would be:

$$i_L = \frac{1}{L}\left(\frac{V_{out}}{n}\right)(t - t_5) + i_{L5} \tag{31}$$

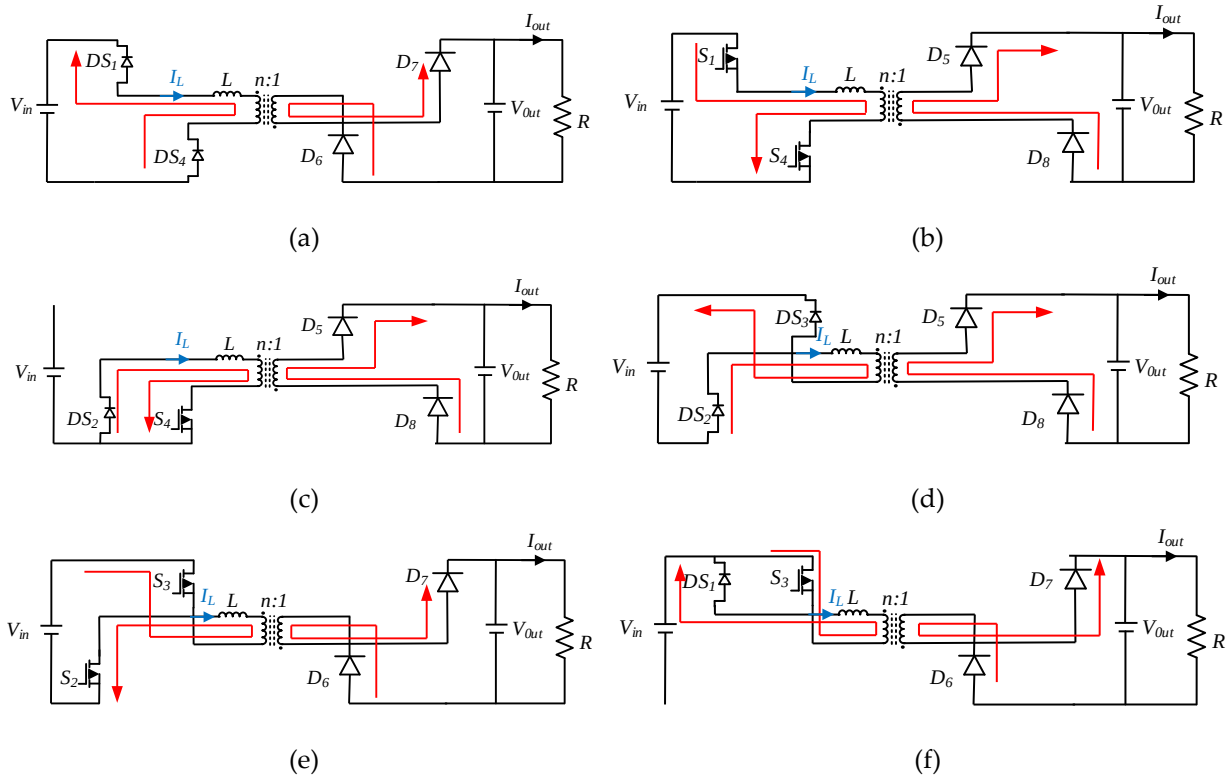

Figure 25. Different operation mode of SAB converter in CCM. (a) cycle (t_0,t_1), (b) cycle (t_1,t_2), (c) cycle (t_2,t_3), (d) cycle (t_3,t_4), (e) cycle (t_4,t_5), (f) cycle (t_5,t_6).

The SAB converters have high output impedance operating in CCM [194]. This behavior is the opposite of the most DC-DC converters in CCM. This is because the inductor is placed on the AC side of the converter and not at the output of the rectifier. Figure 26 shows the inductor in CCM for the SAB converter.

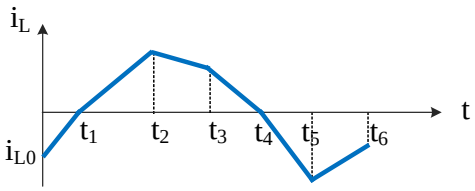

Figure 26. Inductor current in CCM.

Figure 27 shows the SAB converter current tracking performance under the traditional proportional-integral (PI) controller, where I_m is the current reference, I_{out} is the converter output current, and E_{ss} is the steady-state current tracking error. It can be seen that the with a properly

designed PI controller, the SAB converter can track the current command and provide a satisfactory current tracking performance with zero steady-state error.

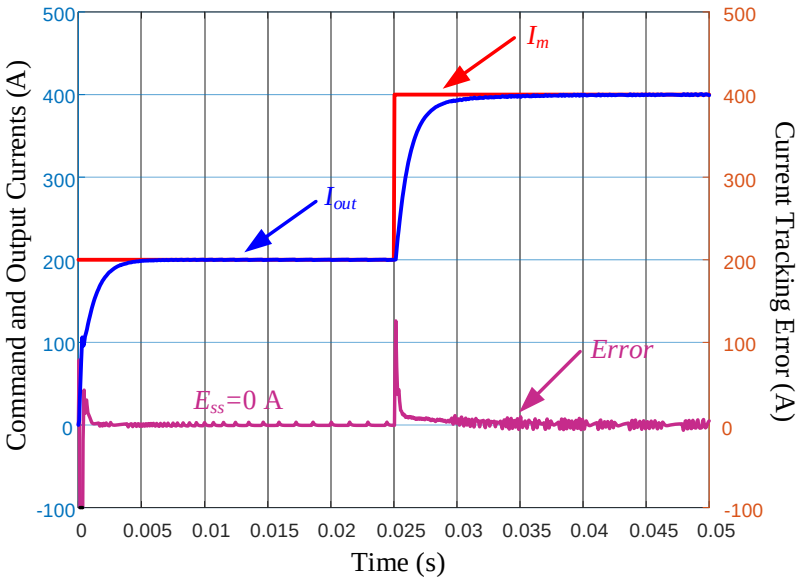

Figure 27. SAB converter current tracking performance.

4.3. DAB Converter Control for Propulsion System

In the proposed MV Figure 14, a DAB DC-DC is one of the options that can be used as a power processing unit for the electric thruster, which offers high efficiency, high power-density, soft-switching, modular and symmetric structure, and controllability [201]. As depicted in Figure 29, the basic design of a DAB converter includes two full-bridge converters, power MOSFETs labeled S_1 through S_8, a transformer's leakage L, which may also incorporate an additional external inductor, and a HF transformer with a turn ratio denoted by n [199]-[201]. The DAB converter gets a fixed input voltage from the MVDC bus, which is presented by V_{bus} in Figure 29, and the output current I_{thrust} is used to drive the electric thruster.

The output current, and hence power of the DAB converter is adjusted by a phase-shift modulation. Figure 28 shows the gate signal S_1 - S_8, transformer voltages V_1 (input) and V_2 (output), and the transformer current (I_L) under the phase-shift control. In the phase-shift control, the duty

cycle of all switches is fixed as 50% [201]. A phase-shift angle D is inserted between the two full-bridge converters switching periods, as shown in Figure 29, where T_{hs} is the half of the switching period. By changing the phase-shift angle, the transformer terminal voltages V_1 and V_2 are controlled, and thus, the transformer current I_L is controlled.

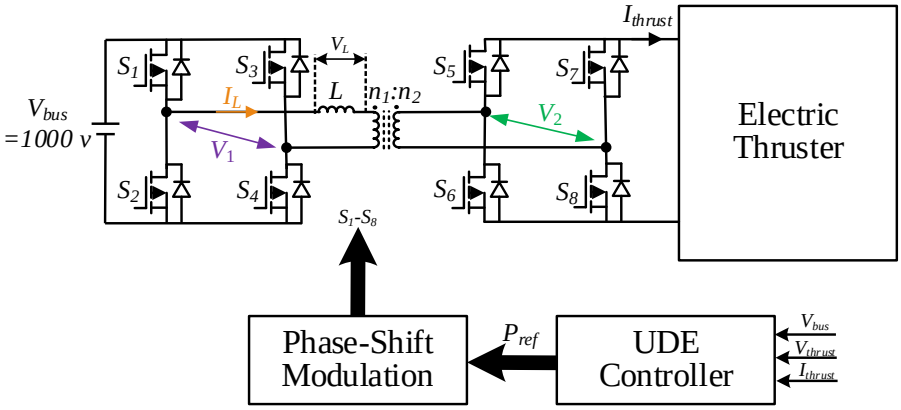

Figure 28. The block diagram of the UDE controlled DAB converters.

In one switching cycle of the phase-shift modulation, there are four switching phases, and in each phase different switches are turned on and different voltages will be applied on the transformer as Figure 29 shows. A detailed description of different switching phases is given as follows.

- In Phase 1, switches S_1, S_4, S_6, and S_7 are turned on, while all other switches are off. It can be seen from the circuit shown in Figure 28 that the transformer voltage is V_1=V_{bus} and V_2=-V_{thrust}, and thus, the transformer leakage inductor voltage V_L = V_{bus} + V_{thrust}.
- In Phase 2, switches S_1, S_4, S_5, and S_8 are turned on, while all other switches are off. The transformer voltage is V_1=V_{bus} and V_2=V_{thrust}, hence V_L = V_{bus} -V_{thrust}.
- In Phase 3, switches S_2, S_3, S_5, and S_8 are turned on, while all other switches are off. The transformer voltage is V_1=-V_{bus} and V_2=V_{thrust}, thus V_L = -V_{bus} -V_{thrust}.

- In Phase 4, switches S_2, S_3, S_6, and S_7 are turned on, while all other switches are off. The transformer voltage is V_1=-V_{bus} and V_2=-V_{thrust}, and thus V_L = -V_{bus} + V_{thrust}.

It can be seen from the switch phase analysis that different voltages will be applied on the transformer at different phases. The transformer current (I_L) rises during Phase 1 and phase 2 due to positive voltage across its inductor and it is reduced in Phase 3 and Phase 4 as the inductor voltage polarity is reversed; this process will repeat in each switching cycle. The DAB converter output power thus can be calculated based on the transformer voltage and current, i.e.,

$$\begin{aligned} P &= \int_0^{2T_{hs}} (V_L \times I_L) dt \\ &= \int_0^{DT_{hs}} [(V_{bus} + V_{thrust}) I_L] dt + \int_{DT_{hs}}^{2T_{hs}} [(V_{bus} - V_{thrust}) I_L] dt \\ &+ \int_{T_{hs}}^{(D+1)T_{hs}} [(-V_{bus} - V_{thrust}) I_L] dt + \int_{(D+1)T_{hs}}^{2T_{hs}} [(-V_{bus} + V_{thrust}) I_L] dt \end{aligned} \tag{32}$$

at different switch phases, the transformer current satisfies,

$$L \frac{dI_L(t)}{dt} = V_L \tag{33}$$

$$\frac{dI_L(t)}{dt} = \begin{cases} \frac{V_{bus} + V_{thrust}}{L}, 0 \le t \le DT_{hs} \text{ (Phase 1)} \\ \frac{V_{bus} - V_{thrust}}{L}, DT_{hs} \le t \le T_{hs} \text{ (Phase 2)} \\ \frac{-V_{bus} - V_{thrust}}{L}, T_{hs} \le t \le (D+1)T_{hs} \text{ (Phase 3)} \\ \frac{-V_{bus} + V_{thrust}}{L}, (D+1)T_{hs} \le t \le 2T_{hs} \text{ (Phase 4)} \end{cases}$$

Combining (32) and (33), the DAB converter output power under the phase-shift control is,

$$P = \frac{nV_{bus}V_{thrust}}{2F_S L} D(1-D) \tag{34}$$

where F_s=1/(2T_{hs}) is the switching frequency of the DAB converter.

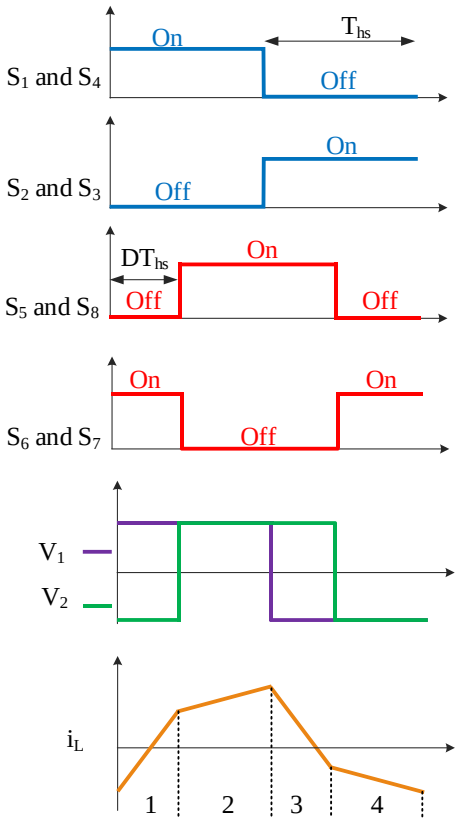

Phase	Conduction Switches	V_L
1	S_1, S_4, S_6, S_7	$V_{bus}+V_{thrust}$
2	S_1, S_4, S_5, S_8	$V_{bus}-V_{thrust}$
3	S_2, S_3, S_5, S_8	$-V_{bus}-V_{thrust}$
4	S_2, S_3, S_6, S_7	$-V_{bus}+V_{thrust}$

Figure 29. SPS modulation on the DAB converter.

In the spacecraft MVDC scheme, Figure 14, the DAB converter output current is regulated by a proposed UDE controller. Referring to Figure 29, based on a current reference I_{cmd}, set by the spacecraft propulsion system, the electrical thruster voltage V_{thrust}, input voltage V_{bus}, and output current I_{thrust}, the UDE controller generates a power reference, P_{ref}, and passes this on to the phase-shift modulation block. Based on (34), the converter output power can be adjusted through changing the phase-shift angle D. In order to track the reference power, i.e. to control the converter output power follow the reference power, the required phase-shift angle D can be calculated as,

$$D = \frac{1 - \sqrt{1 - \frac{8F_s L P_{ref}}{(nV_{bus}V_{thrust})}}}{2} \tag{35}$$

As mentioned earlier, the UDE controller will achieve the output current tracking and reject disturbance through adjusting the reference power P_{ref}. According to principles of electrical circuits, the output power is governed by,

$$P_{ref} = V_{thrust} I_{thrust} + f \tag{36}$$

where f is the system uncertainty and disturbance. Based on (36), the converter output current can be written as,

$$I_{thrust} = \frac{P_{ref} - f}{V_{thrust}} \tag{37}$$

In order to let the output current track the command current, i.e., I_{thrust}=I_{cmd}, the reference power should satisfy,

$$P_{ref} = V_{thrust} I_{cmd} + f \tag{38}$$

The system disturbance can be represented by,

$$f = P_{ref} - (V_{thrust} I_{thrust}) \tag{39}$$

Similar to the boost converter disturbance estimation, the DAB converter disturbance is estimated as,

$$f_{est} = G_f \left(P_{ref} - (V_{thrust} I_{thrust}) \right) \tag{40}$$

Within the bandwidth of G_f,

$$f_{est} = G_f . f \approx f \tag{41}$$

Thus, the UDE-based DAB converter current controller is derived as,

$$P_{ref} = V_{thrust} I_{cmd} + f_{est} \tag{42}$$

Figure 30 shows the control performance of the DAB converter. The DAB converter is used to drive the electrical thruster. The DAB converter output current should track the current command. The current tracking performance when the disturbance estimation filter G_f is zero

and only the state-feedback control is enabled has been indicated in the figure. It can be seen that the steady-state tracking error of the DAB current control is not zero due to system uncertainty and disturbances.

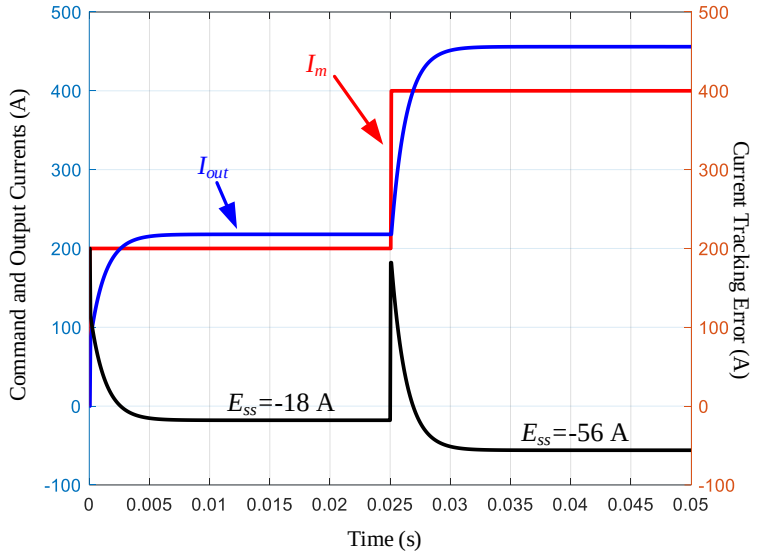

Figure 30. Current mode DAB converter tracking performance under the UDE controller while the reference system bandwidth is 200 Hz with no disturbance estimation filter.

After implementing the filter G_f, as Figure 31 depicts, the disturbance and uncertainty can be effectively attenuated, and the steady-state current tracking error is zero. Also, it can be seen from the figure that the tracking error converge within 3ms, which suggested satisfactory transient performance as well.

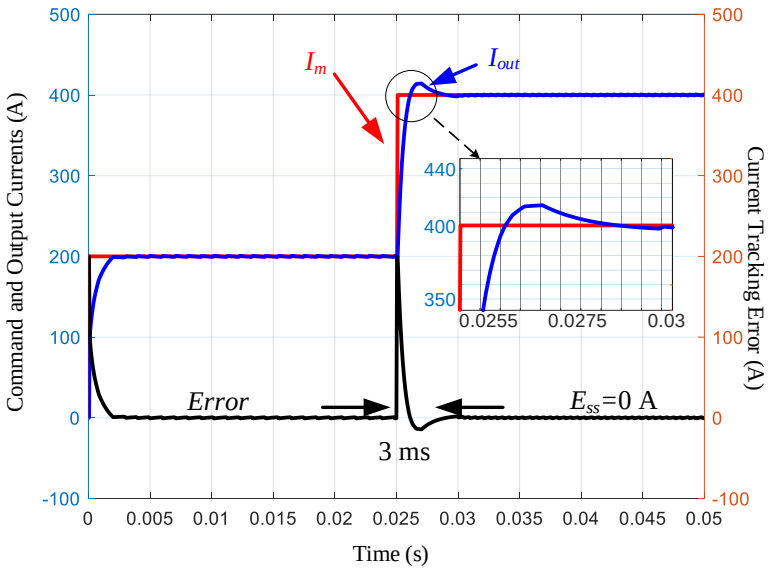

Figure 31. Current mode DAB converter tracking performance under the UDE controller while the reference system bandwidth is 200 Hz and G_f is 200 Hz when the circuit parameters are accurate.

Similar to the simulation of the boost converter, the circuit parameter uncertainty must be considered in real applications. Figures 32(a) and 32(b) demonstrate that the proposed control scheme can maintain satisfactory control performance even under ±20% parameter uncertainty. It can be seen that the proposed UDE control scheme can maintain the system stability and robustness even under large system uncertainties. Overall, both the boost converter simulation and the DAB converter simulation have demonstrated the effectiveness of the proposed schemes.

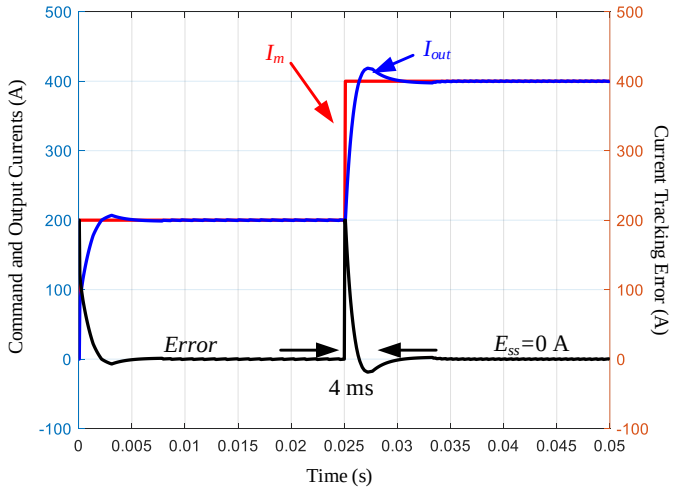

(a)

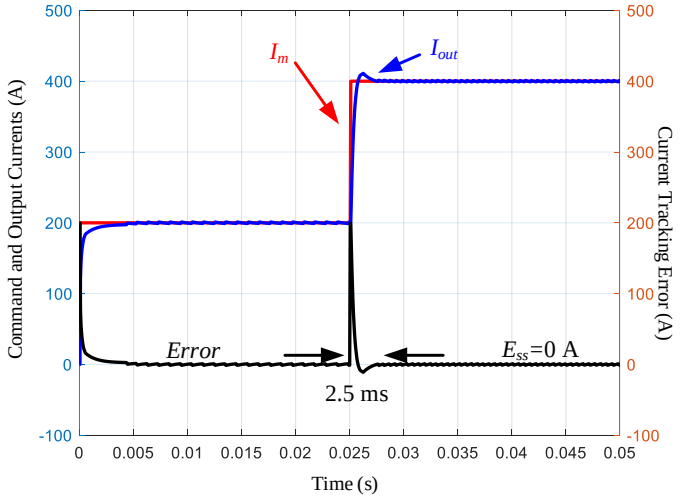

(b)

Figure 32. Current mode DAB converter tracking performance under the UDE controller while the reference system bandwidth is 200 Hz. (a) Bandwidth of G_f is 200 Hz when the circuit parameters have +20% error; and (b) Bandwidth of G_f is 200 Hz when the circuit parameters have -20% error.

5. CONCLUSION AND FUTURE WORK

In this work, a MVDC system with MW-scale spacecraft power and propulsion for Mars mission is proposed. The proposed MVDC system contains an NEP to provide heat source to the PM generator for electricity production, a PV source, and a BESS as a backup energy source. In order to achieve the power transmission among those energy sources, boost converters and isolated DC-DC converter are implemented in the proposed MVDC system.

The PV panels were interfaced to the MVDC bus using a unidirectional boost DC-DC converter. The rationale behind this choice is that solar panels typically only need to supply power to the system and do not require the capability to absorb power. The unidirectional converter efficiently converts the variable output voltage of the PV panels to the higher, stable voltage level required by the MVDC bus, optimizing the utilization of solar energy. By using a unidirectional converter for the PV panels, the system complexity and cost are reduced while still ensuring that the solar energy is effectively harnessed to support the spacecraft's power needs. On the other hand, for the BESS, a bidirectional DC-DC boost converter was selected to facilitate the seamless flow of energy in both directions. This bidirectionality is essential for the BESS, as it allows the battery to not only supply power to the spacecraft's low-voltage power system and payload when needed but also to be recharged from the MVDC bus when excess energy is available. This dual functionality ensures that the BESS can effectively act as a backup power source, enhancing the overall reliability and flexibility of the spacecraft's power system.

The MVDC system stability and robustness can be impacted by system disturbance and uncertainty. To enhance the system performance, UDE based current control schemes are proposed for the boost converters. The proposed scheme is capable of actively estimating and compensating for system uncertainties and disturbances, thereby enhancing the control performance and

robustness of the system. The control system consistently meets the reference current without persistent deviation. The zero steady state error indicates the ability of the controller to maintain accuracy and stability in the long-term.

In the analysis of the isolated DC-DC converters for the spacecraft's power architecture, both the SAB and DAB converters were evaluated for their performance in connecting to the electric thrusters. The SAB converter, controlled by a PI controller, demonstrated satisfactory current tracking performance. With a properly designed PI controller, the SAB converter was able to track the current reference accurately, providing zero steady-state error and ensuring efficient power transfer to the thrusters.

The DAB converter, equipped with the proposed UDE control scheme, exhibited robust performance under significant parameter uncertainties. The UDE control scheme successfully maintained system stability and robustness, even under ±20% parameter variations, highlighting its effectiveness in handling large system uncertainties.

The analysis of the isolated DC-DC converters for the spacecraft's power architecture has demonstrated the distinct advantages of both the SAB and DAB converters. The SAB converter, with its satisfactory current tracking capability, provides a cost-effective solution for the power management system, particularly suitable for applications where budget constraints are a primary concern. Whereas, the DAB converter, with its robust performance under uncertainties and its ability to control power flow bidirectionally, offers a versatile solution for feeding DC/AC loads under conditions when power availability is limited. Additionally, the DAB converter's capability to provide higher power density makes it an attractive option for scenarios requiring compact and efficient power conversion.

Future research could build on the current work by delving deeper into the causes of high-frequency oscillations within MVDC systems. The aim would be to develop more advanced estimation and control schemes that go beyond disturbance rejection and target the mitigation of such oscillations. Analyzing the frequency response of the system impedances in greater detail could provide new insights into resonance phenomena and their impact on system stability.

While this thesis focused on the small-signal analysis for controller design, subsequent studies could extend to include large-signal analysis. This expansion would allow for a comprehensive understanding of the boost converter's behavior under a wide range of operating conditions, including startup, shutdown, and extreme variations in load and input conditions.

Investigating different converter topologies used for low power applications presents a significant opportunity for the future work of the large spacecraft power system. This work could focus on optimizing converter design for efficiency and size, particularly for applications where space and weight are critical constraints.

Building upon the foundation laid by this thesis, the suggested areas for future work promise to advance our understanding and capabilities in spacecraft power systems, paving the way for more resilient, and efficient energy management in the ever-evolving field of space exploration.

REFERENCES

[1] Arunan, Subbiah, and R. Satish. "Mars Orbiter Mission spacecraft and its challenges." Current Science (2015): 1061-1069.

[2] Rivellini, Tommaso. "The challenges of landing on Mars." Frontiers in Engineering: Reports on Leading-Edge Engineering from the 2004 NAE Symposium on Frontiers of Engineering. 2005.

[3] Starek, Joseph A., et al. "Spacecraft autonomy challenges for next-generation space missions." Advances in control system technology for aerospace applications. Berlin, Heidelberg: Springer Berlin Heidelberg, 2015. 1-48.

[4] Loeb, H. W., et al. "A realistic concept of a manned Mars mission with nuclear–electric propulsion." Acta Astronautica 116 (2015): 299-306.

[5] Willson, D., and J. D. A. Clarke. "A practical architecture for exploration-focused manned Mars missions using chemical propulsion, solar power generation and in-situ resource utilisation." Proceedings of the 6th Australian Space Science Conference. 2006.

[6] N. Barba et al., "Mars Small Spacecraft Studies: Overview," 2019 IEEE Aerospace Conference, Big Sky, MT, USA, 2019, pp. 1-10.

[7] Balint, Tibor S. "Comparison of power system options between future lunar and mars missions." International Lunar Conference 2005 Proceedings. 2005.

[8] “Launch Vehicle.” Wikipedia, 6 Mar. 2022, en.wikipedia.org/wiki/Launch_vehicle. Accessed 26 Nov. 2022.

[9] M. R. Patel, O. Beik, Spacecraft Power Systems. CRC Press, 2023.

[10] Turner, Martin JL. Rocket and spacecraft propulsion: principles, practice and new developments. Springer Science & Business Media, 2008.

[11] Czysz, Paul A., Claudio Bruno, and Bernd Chudoba. Future Spacecraft Propulsion Systems and Integration. Springer: Berlin/Heidelberg, Germany, 2018.

[12] W. Chen, S. Zhang and V. Dinavahi, "Real-Time ML-Assisted Hardware-in-the-Loop Electro-Thermal Emulation of LVDC Microgrid on the International Space Station," IEEE Open Journal of Power Electronics, vol. 3, pp. 168-181, 2022.

[13] K. B. Chin et al., "Energy Storage Technologies for Small Satellite Applications," Proceedings of the IEEE, vol. 106, no. 3, pp. 419-428, March 2018.

[14] B. Saude, N. LaSart, J. Blair and O. Beik, "Microgrid-Based Wind and Solar Power Generation on Moon and Mars," IEEE Transactions on Smart Grid, vol. 14, no. 2, pp. 1329-1332, March 2023.

[15] “Irradiance and PV Performance Optimization | AE 868: Commercial Solar Electric Systems.” Www.e-Education.psu.edu, www.e-education.psu.edu/ae868/node/877.

[16] Q. Yang, Y. Yang, R. Li, Y. Dou, B. Dong and A. Yang, "An Analog-Device-Based Five-Domain Control Method and Distributed System Configuration for High-Power Spacecraft Power Systems," in IEEE Journal of Emerging and Selected Topics in Power Electronics, vol. 10, no. 5, pp. 5332-5344, Oct. 2022.

[17] W. Jie, W. Li, W. Jianchao, H. Xiong, C. Yonggang and L. Huiyao, "Matching Design Method of SSPC and Fuse Used in Series in Spacecraft Power Distribution System," 2022 4th International Conference on Smart Power & Internet Energy Systems (SPIES), Beijing, China, 2022, pp. 1586-1590.

[18] K. G. Boggs, K. Goodliff and D. Elburn, "Capabilities Development: From International Space Station and the Moon to Mars," 2020 IEEE Aerospace Conference, Big Sky, MT, USA, 2020, pp. 1-10.

[19] M. A. Carbone, A. Sajadi, J. M. Murray, J. T. Csank and K. A. Loparo, "Voltage Stability of Spacecraft Electric Power Systems for Deep Space Exploration," in IEEE Access, vol. 11, pp. 38828-38839, 2023.

[20] Azari, A. N., Soleymani, S., Mozafari, B., & Sarfi, G. (2018). Optimal transmission congestion management with V2G in smart grid. American Journal of Electrical Power and Energy Systems, 7(2), 16-24.

[21] Jorgensen, Catherine A., and Jeffrey Antol. International space station evolution data book. No. NASA/SP-2000-6109/VOL1/REV1. 2000.

[22] Thirsk, Robert, et al. "The space-flight environment: the International Space Station and beyond." Cmaj 180.12 (2009): 1216-1220.

[23] International Space Station Basics- NASA. (Online) https://www.nasa.gov/wp-content/uploads/2012/01/179225main_iss_poster_back.pdf?emrc=c7bee6

[24] International Space Station Familiarization, Johnson Space Center, TD9702A, Houston, TX, 1998.

[25] Lambright, W. Henry. "Administrative leadership and long-term technology: NASA and the international space station." Space Policy 47 (2019): 85-93.

[26] Schwanbeck, Eugene R. "Advanced Solar Arrays on the ISS." Association of Space Explorers (ASE) Planetary Congress 2019. No. JSC-E-DAA-TN74083. 2019.

[27] NASA. (2023, September 27). International Space Station Facts and Figures. NASA. https://www.nasa.gov/international-space-station/space-station-facts-and-figures/

[28] Thomas, L. Dale. "System engineering the international space station." NASA Langley Research Center, International Space Station Video Conference. Vol. 97. 1997.

[29] Salmond, Wendy, Justin Walsh, and Alice Gorman. "Eternity in low earth orbit: Icons on the international space station." Religions 11.11 (2020): 611.

[30] Wright Jr, Kenneth H., et al. "ROSA and Solar Cell Module Combined Environments Test Plan." 16th Spacecraft Charging and Technology Conference. 2022.

[31] Dalton, Penni J. "International Space Station Lithium-Ion Battery Safety Considerations." IEEE Huntsville Power and Energy Society. 2021.

[32] Anand, M. Dev, et al. "Lithium-ion cells for space applications: Aspects of durability." Advances in Space Research 72.7 (2023): 2948-2958.

[33] Shirobokov, Maksim, Sergey Trofimov, and Mikhail Ovchinnikov. "Survey of machine learning techniques in spacecraft control design." Acta Astronautica 186 (2021): 87-97.

[34] Harris, G., Ping He, and O. Abdelkhalik. "Control co-design optimization of spacecraft trajectory and system for interplanetary missions." Journal of Spacecraft and Rockets (2023).

[35] Xie, Yongchun, et al. Spacecraft dynamics and control. Singapore: Springer, 2022.

[36] Chai, Runqi, et al. "Review of advanced guidance and control algorithms for space/aerospace vehicles." Progress in Aerospace Sciences 122 (2021): 100696.

[37] Rigo, Cezar Antônio, et al. "Task scheduling for optimal power management and quality-of-service assurance in CubeSats." Acta Astronautica 179 (2021): 550-560.

[38] Ferre, Ruben Morales, and Elena Simona Lohan. "Comparison of MEO, LEO, and terrestrial IoT configurations in terms of GDOP and achievable positioning accuracies." IEEE Journal of Radio Frequency Identification 5.3 (2021): 287-299.

[39] Williamsen, J., and Evans, S. “Orbital Debris Momentum Transfer in Satellite Shields following Hypervelocity Impact, and Its Application to Environment Validation.” Paper 102 presented at the 14th Hypervelocity Impact Symposium, Canterbury, Kent, UK, April 26, 2017.

[40] Squire, M., et al., 2014. Joint Polar Satellite System Micrometeoroid and Orbital Debris (MMOD) Assessment, NASA Engineering and Safety Council (NESC) Study TI-15-xxxxx, September 2016

[41] Squire, M., et al. “Evaluation of Micrometeoroid and Orbital Debris (MMOD) Risk Predictions with Available On-Orbit Assets” (NESC-RP-14-01000). Hampton, VA: NASA Engineering and Safety Center, September 1, 2017.

[42] O. Beik, M. R. Patel and S. Talebzadeh, "Large Spacecraft Electric Propulsion Using Multiphase Generator," 2023 IEEE Aerospace Conference, Big Sky, MT, USA, 2023, pp. 1-8.

[43] Kumar V, Paraschivoiu M, Paraschivoiu I. Low Reynolds Number Vertical Axis Wind Turbine for Mars. Wind Engineering. 2010;34(4):461-476.

[44] C. Holstein-Rathlou, P. Thomas, J. Merrison, J. Iversen, Wind turbine power production under current Martian atmospheric conditions, in: Mars Workshop on Amazonian and Present Day Climate, Vol. 2086, 2018, p. 4004.

[45] Rucker, Michelle. Integrated surface power strategy for Mars. No. JSC-CN-32561. 2015.

[46] McClure, Kevin R. and Paige N. Eppenstein Anderson. "An Uneven Playing Field: Fundraising at Regional Public Universities in the Aftermath of the Great Recession." Philanthropy & Education, vol. 3 no. 2, 2020, p. 1-26. Project MUSE.

[47] Cubas, Javier, Santiago Pindado, and Marta Victoria. "On the analytical approach for modeling photovoltaic systems behavior." Journal of power sources 247 (2014): 467-474.

[48] Pindado, Santiago, and Javier Cubas. "Simple mathematical approach to solar cell/panel behavior based on datasheet information." Renewable energy 103 (2017): 729-738.

[49] Cubas, J.; Pindado, S.; Sorribes-Palmer, F. Analytical Calculation of Photovoltaic Systems Maximum Power Point (MPP) Based on the Operation Point. Appl. Sci. 2017, 7, 870.

[50] Javier Cubas, Santiago Pindado, Ángel Sanz-Andrés, "Accurate Simulation of MPPT Methods Performance When Applied to Commercial Photovoltaic Panels", The Scientific World Journal, vol. 2015, Article ID 914212, 16 pages, 2015.

[51] Cubas, J.; Pindado, S.; De Manuel, C. Explicit Expressions for Solar Panel Equivalent Circuit Parameters Based on Analytical Formulation and the Lambert W-Function. Energies 2014, 7, 4098-4115.

[52] Oral, Ahmet Yavuz, Zehra Banu Bahsi, and Mehmet Ozer. "International Congress on Energy Efficiency and Energy Related Materials (ENEFM2013)." International Congress on Energy Efficiency and Energy Related Materials (ENEFM2013): Proceedings. Vol. 155. 2014.

[53] Roibás-Millán, Elena, et al. "Testing solar panels for small-size satellites: the UPMSAT-2 mission." Measurement Science and Technology 28.11 (2017): 115801.

[54] Pindado, S.; Cubas, J.; Roibás-Millán, E.; Bugallo-Siegel, F.; Sorribes-Palmer, F. Assessment of Explicit Models for Different Photovoltaic Technologies.

[55] Bale, S. D., et al. "Dust impact voltage signatures on Parker Solar Probe: influence of spacecraft floating potential." arXiv preprint arXiv:2006.00776 (2020).

[56] Bhavani, Munipally, et al. "Impact of variation of solar irradiance and temperature on the inverter output for grid connected photo voltaic (PV) system at different climate conditions." Materials Today: Proceedings 80 (2023): 2101-2108.

[57] Farley, Kenneth A., et al. "Mars 2020 mission overview." Space Science Reviews 216 (2020): 1-41.

[58] Madhavan, B. L., and M. Venkat Ratnam. "Impact of a solar eclipse on surface radiation and photovoltaic energy." Solar Energy 223 (2021): 351-366.

[59] National Academies of Sciences, Engineering, and Medicine. Space nuclear propulsion for human mars exploration. 2021.

[60] R. K. Tripathi and J. E. Nealy, "Mars Radiation Risk Assessment and Shielding Design for Long-Term Exposure to Ionizing Space Radiation," 2008 IEEE Aerospace Conference, Big Sky, MT, USA, 2008, pp. 1- 9.

[61] E. Y. Choueiri, "A Critical History of Electric Propulsion: The First 50 Years (1906-1956)," J. Propuls. Power, vol. 20, no. 2, pp. 193–203, 2004.

[62] M. D. Kankam and M. E. Elbuluk, "A survey of power electronics applications in aerospace technologies," Proc. Intersoc. Energy Convers. Eng. Conf., vol. 1, no. November, pp. 147–153, 2001.

[63] M. Turner, Rocket and Spacecraft Propulsion: Principles, Practice and New Developments. 2009.

[64] R. H. Frisbee, "Advanced Space Propulsion for the 21st Century," J. Propuls. Power, vol. 19, no. 6, pp. 1129–1154, 2003.

[65] B. Jorns, I. Mikellides, S. Mazouffre, and H. Koizumi, "Physics of electric propulsion," J. Appl. Phys., vol. 132, no. 11, 2022.

[66] C. Charles, "Plasmas for spacecraft propulsion," J. Phys. D. Appl. Phys., vol. 42, no. 16, 2009.

[67] C. Charles, R. W. Boswell, and K. Takahashi, "Investigation of radiofrequency plasma sources for space travel," Plasma Phys. Control. Fusion, vol. 54, no. 12, 2012.

[68] D. Goebel and I. Katz, Fundamentals of Electric Propulasion: Ion and Hall Thrusters. 2008.

[69] L. Garrigues and P. Coche, "Electric propulsion: Comparisons between different concepts," Plasma Phys. Control. Fusion, vol. 53, no. 12, 2011.

[70] M. Martinez-Sanchez and J. Pollard, "Spacecraft Electric Propulsion-An Overview," J. Propuls. Power - J PROPUL POWER, vol. 14, pp. 688–699, 1998.

[71] E. Ahedo, "Plasmas for space propulsion," Plasma Phys. Control. Fusion, vol. 53, no. 12, 2011.

[72] D. Krejci and P. Lozano, "Space Propulsion Technology for Small Spacecraft," Proc. IEEE, vol. 106, no. 3, pp. 362–378, 2018.

[73] D. Djamal, K. Mohamed, and A. Rüstem Aslan, “RESISTOJET Propulsion System for Small Satellite,” in 2019 9th International Conference on Recent Advances in Space Technologies (RAST), 2019, pp. 159–166.

[74] R. Ranjan, S. Chou, F. Riaz and K. Karthikeyan, "Cold gas micro propulsion development for satellite application", Energy Procedia, vol. 143, pp. 754-761, 2017

[75] D. R. Jovel, M. L. R. Walker, and D. Herman, “Review of High Power Electrostatic and Electrothermal Electric Propulsion,” J. Propuls. Power, vol. 38, no. 6, pp. 1051–1081, 2022.

[76] K. Polzin, A. Martin, J. Little, C. Promislow, B. Jorns, and J. Woods, “State-of-the-Art and Advancement Paths for Inductive Pulsed Plasma Thrusters,” Aerospace, vol. 7, p. 105, 2020.

[77] Polzin, Kurt A. "Comprehensive review of planar pulsed inductive plasma thruster research and technology." Journal of Propulsion and Power 27.3 (2011): 513-531.

[78] Polzin, Kurt, Millard Rose, and Robert Miller. "Laboratory-model integrated-system FARAD thruster." 44th AIAA/ASME/SAE/ASEE Joint Propulsion Conference & Exhibit. 2008.

[79] NASA –Ion Propulsion, [Online]. https://www.nasa.gov/centers/glenn/about/fs21grc.html. Accessed May 2023.

[80] O. O. Baranov, U. Cvelbar, and K. Bazaka, “Concept of a Magnetically Enhanced Vacuum Arc Thruster With Controlled Distribution of Ion Flux,” IEEE Trans. Plasma Sci., vol. 46, no. 2, pp. 304–310, 2018.

[81] Krause, Frederick C., et al. "High specific energy lithium primary batteries as power sources for deep space exploration." Journal of the Electrochemical Society 165.10 (2018): A2312.

[82] Asundi, Sharan A., and Norman G. Fitz-Coy. "CubeSat mission design based on a systems engineering approach." 2013 IEEE Aerospace Conference. IEEE, 2013.

[83] Yeo, Suk Hyun, et al. "Miniaturization perspectives of electrostatic propulsion for small spacecraft platforms." Progress in Aerospace Sciences 126 (2021): 100742.

[84] Wang, Yu-Shin, and Shyh-Jong Chung. "A miniature quadrifilar helix antenna for global positioning satellite reception." IEEE transactions on antennas and propagation 57.12 (2009): 3746-3751.

[85] Shair, R. C., et al. "A review of batteries and fuel cells for space power systems." Journal of Spacecraft and Rockets 4.7 (1967): 833-838.

[86] Burke, Kenneth. "Fuel cells for space science applications." 1st International Energy Conversion Engineering Conference (IECEC). 2003.

[87] Hacker, Barton C., and James M. Grimwood. On the shoulders of Titans: A history of Project Gemini. Vol. 4203. National Aeronautics and Space Administration, Scientific and Technical Information Division, Office of Technology Utilization, 1977.

[88] Siemers III, Paul M., and Terry J. Larson. "Space shuttle orbiter and aerodynamic testing." Journal of Spacecraft and Rockets 16.4 (1979): 223-231.

[89] O'Brien, R. C., et al. "Safe radioisotope thermoelectric generators and heat sources for space applications." Journal of Nuclear Materials 377.3 (2008): 506-521.

[90] Ritz, Fred, and Craig E. Peterson. "Multi-mission radioisotope thermoelectric generator (MMRTG) program overview." 2004 IEEE aerospace conference proceedings (IEEE Cat. No. 04TH8720). Vol. 5. IEEE, 2004.

[91] Whiting, Christofer E. "Empirical performance analysis of MMRTG power production and decay." 2020 IEEE Aerospace Conference. IEEE, 2020.

[92] Rucker, Michelle A., et al. "NASA's Strategic Analysis Cycle 2021 (SAC21) Human Mars Architecture." 2022 IEEE Aerospace Conference (AERO). IEEE, 2022.

[93] Braun, Robert, Roger Myers, and S. Bragg-Sitton. "Space nuclear propulsion for human mars exploration." NASEM Space Nuclear Propulsion Technologies Committee Report. Washington, DC: National Academies of Sciences, Engineering and Medicine (2021).

[94] Polzin, Kurt A., et al. "Strategy for developing technologies for megawatt-class nuclear electric propulsion systems." 2022 International Electric Propulsion Conference. No. IEPC-2022-155. 2022.

[95] M. Duchek et al., "Hybrid NEP-Chemical Vehicle and Propulsion Technology Study for Crewed Mars Missions," 2021.

[96] Merrill, Raymond G., et al. "Mars conjunction crewed missions with a reusable hybrid architecture." 2015 IEEE Aerospace Conference. IEEE, 2015.

[97] Chai, Patrick, Min Qu, and Bianca Saputra. "Human Mars Mission In-Space Transportation Sensitivity for Nuclear Electric/Chemical Hybrid Propulsion." AIAA Propulsion and Energy 2021 Forum. 2021.

[98] Adam K. Martin, Kurt A. Polzin, Francis M. Curran, Roger M. Myers, and Mitchell A. Rodriguez. "A Technology Maturation Plan for the Development of Nuclear Electric Propulsion," Joint Army-Navy-NASA-Air Force (JANNAF) Meeting, 2022.

[99] D. Nikitaev, D. C. Smith, M. Duchek, C. Harnack, W. Machemer, and G. Emanuel. "Nuclear Electric Propulsion Modular Power Conversion Model," Nuclear and Emerging Technologies for Space, 2022.

[100] Vasilieva, Tatiana M., and Michael N. Vasiliev. "Hybrid Plasmas Generation Inside Dielectric Containers." IEEE Transactions on Plasma Science 49.11 (2021): 3307-3316.

[101] Bennett, Gary L. "Introduction to space nuclear power and propulsion." Encyclopedia of Nuclear Energy. Elsevier (2021): 155-167.

[102] Dyson, Rodger, et al. Nuclear electric propulsion brayton power conversion working fluid considerations. No. E-20018. 2022.

[103] Lee S. Mason, Dynamic Energy Conversion: Vital Technology for Space Nuclear Power, Journal of Aerospace Engineering, Vol. 26, 2014.

[104] Wang, L., Lin, X., Zhang, H., Peng, L., Zhang, X., & Chen, H. (2022). Analytic optimization of Joule–Brayton cycle-based pumped thermal electricity storage system. Journal of Energy Storage, 47, 103663.

[105] CLIQUET-MORENO, Elisa & Jansen, Frank & POIDOMANI, Gaetano & RUAULT, Jean-Marc & Worms, Jean-Claude. (2012). MEGAHIT: Megawatt Highly Efficient Technologies for Space Power and Propulsion Systems for Long-duration Exploration Missions - A Supporting Action for H2020 EC programme.

[106] D. Nikitaev, M. E. Duchek, C. Harnack, W. Machemer, and D. Rao, “Heat Pipe Heat Exchanger for Nuclear Electric Propulsion Power Conversion System,” 2022.

[107] C. Harnack, W. Machemer, D. Nikitaev, and M. Duchek, “Component-level Performance and Mass Sensitivity Analysis of NEP MW-class Power System,” in ASCEND 2022.

[108] Reynolds, C. B., Joyner, C. R., Kokan, T. S., & Levack, D. J. (2022). Power Management and Distribution System Trades for an NEP-Based Human Mars Mission. In ASCEND 2022 (p. 4217).

[109] J. Slough, "Manned Spacecraft Propulsion through Direct Conversion of Nuclear Energy," 2022 IEEE Aerospace Conference (AERO), Big Sky, MT, USA, 2022, pp.1-13.

[110] Y. Lei, Y. Han and Y. Yang, "Design of Deep Space Electric Propulsion Spacecraft Power System," 2023 6th International Conference on Energy, Electrical and Power Engineering (CEEPE), Guangzhou, China, 2023, pp. 873- 878.

[111] Thanikanti, Sudhakar Babu, et al. "A dynamic mismatch loss mitigation algorithm with dual input dual output converter for solar PV systems." Solar Energy Materials and Solar Cells 251 (2023): 112163.

[112] Kasper, Matthias, Dominik Bortis, and Johann W. Kolar. "Classification and comparative evaluation of PV panel-integrated DC–DC converter concepts." IEEE Transactions on Power Electronics 29.5 (2013): 2511-2526.

[113] Hajela, Gyan, Fred Cohen, and Penni Dalton. "Reconditioning of Batteries on the International Space Station." 2nd International Energy Conversion Engineering Conference. 2004.

[114] D. Divan and P. Kandula, “Distributed power electronics: an enabler for the future grid,” in CPSS Transactions on Power Electronics and Applications, vol.1, no.1, pp. 57–65, Dec. 2016.

[115] Y. Yang, A. Sangwongwanich, and F. Blaabjerg, “Design for reliability of power electronics for grid-connected photovoltaic systems,” in CPSS Transactions on Power Electronics and Applications, vol.1, no.1, pp.92– 103, Dec. 2016.

[116] Q. Mei, M. Shan, L. Liu, and J. M. Guerrero, “A novel improved variable step-size incremental-resistance MPPT method for PV systems,” in IEEE Transactions on industrial Electronics, vol. 58, no. 6, pp. 2427–2434, Jun. 2011.

[117] Y. Jiang, J. A. Abu Qahouq, and T. A. Haskew, “Adaptive step size with adaptive-perturbation-frequency digital MPPT controller for a singlesensor photovoltaic solar system,” in IEEE Transactions on Power Electronics, vol. 28, no. 7, pp. 3195–3205, Jul. 2013.

[118] Gietl, Eric B., et al. "The electric power system of the International Space Station-a platform for power technology development." 2000 IEEE Aerospace Conference. Proceedings (Cat. No. 00TH8484). Vol. 4. IEEE, 2000.

[119] M. A. Abdourraziq, M. Maaroufi, and M. Ouassaid, “A new variable step size INC MPPT method for PV systems,” in Proceedings of 2014 International Conference on Multimedia Computing and Systems (ICMCS), Marrakech, 2014, pp. 1563–1568.

[120] M. A. Elgendy, B. Zahawi, and D. J. Atkinson, “Comparison of directly connected and constant voltage controlled photovoltaic pumping systems,” in IEEE Transactions on Sustainable Energy, vol. 1, no. 3, pp. 184–192, Oct. 2010.

[121] P. S. Samrat, F. F. Edwin, and W. Xiao, “Review of current sensorless maximum power point tracking technologies for photovoltaic power systems,” in Proceedings of 2013 International Conference on Renewable Energy Research and Applications (ICRERA), Madrid, 2013, pp. 862–867.

[122] I. S. Kim, M. B. Kim, and M. J. Youn, “New maximum power point tracker using sliding-mode observer for estimation of solar array current in the grid-connected photovoltaic system,” in IEEE Transactions on Industrial Electronics, vol. 53, no. 4, pp. 1027–1035, Jun. 2006.

[123] S. C. Ferreira, R. B. Gonzatti, R. R. Pereira, C. H. da Silva, L. E. B. da Silva, and G. Lambert-Torres, “Finite control set model predictive control for dynamic reactive power compensation with hybrid active power filters,” in IEEE Transactions on Industrial Electronics, vol. 65, no. 3, pp. 2608–2617, Mar. 2018.

[124] S. Sajadian and R. Ahmadi, “Model predictive-based maximum power point tracking for grid-tied photovoltaic applications using a Z-source inverter,” in IEEE Transactions on Power Electronics, vol. 31, no. 11, pp. 7611–7620, Nov. 2016.

[125] O. Abdel-Rahim, H. Funato, and J. Haruna, “Novel predictive maximum power point tracking techniques for photovoltaic applications,” in Journal Power Electronics, vol. 16, no. 1, pp. 277–286, 2016.

[126] Abdel-Salam, Mazen, Mohamed Th El-Mohandes, and Mahmoud El-Ghazaly. "An efficient tracking of MPP in PV systems using a newly-formulated P&O-MPPT method under varying irradiation levels." Journal of Electrical Engineering & Technology 15 (2020): 501-513.

[127] Chen, S. Zhang and V. Dinavahi, "Real-Time MLAssisted Hardware-in-the-Loop Electro-Thermal Emulation of LVDC Microgrid on the International Space Station," IEEE Open Journal of Power Electronics, vol. 3, pp. 168-181, 2022.

[128] Raiker, Gautam A., and Umanand Loganathan. "Current control of boost converter for PV interface with momentum-based perturb and observe MPPT." IEEE Transactions on Industry Applications 57.4 (2021): 4071-4079.

[129] Chen, Yuqing, et al. "A review of lithium-ion battery safety concerns: The issues, strategies, and testing standards." Journal of Energy Chemistry 59 (2021): 83-99.

[130] Yayathi, Sandeep, et al. "Energy distributions exhibited during thermal runaway of commercial lithium ion batteries used for human spaceflight applications." Journal of Power Sources 329 (2016): 197-206.

[131] Zhou, Long, et al. "State estimation models of lithium-ion batteries for battery management system: status, challenges, and future trends." Batteries 9.2 (2023): 131.

[132] Lami, Mahmoud, Abdulrahim Shamayleh, and Shayok Mukhopadhyay. "Minimizing the state of health degradation of Li-ion batteries onboard low earth orbit satellites." Soft Computing 24 (2020): 4131-4147.

[133] Martí-Florences, Miquel, Andreu Cecilia, and Ramon Costa-Castelló. "Modelling and estimation in lithium-ion batteries: A literature review." Energies 16.19 (2023): 6846.

[134] Song, Yuchen, Yu Peng, and Datong Liu. "Model-based health diagnosis for lithium-ion battery pack in space applications." IEEE Transactions on Industrial Electronics 68.12 (2020): 12375-12384.

[135] Shiau, Jaw-Kuen, and Chien-Wei Ma. "Li-ion battery charging with a buck-boost power converter for a solar powered battery management system." Energies 6.3 (2013): 1669-1699.

[136] Ramkumar, M. Siva, et al. "Review on Li-Ion Battery with Battery Management System in Electrical Vehicle." Advances in Materials Science and Engineering 2022 (2022).

[137] K. Wang, F.C. Lee, and J. S. Lai, “Operation principles of bidirectional full-bridge dc/dc converter with unified soft-switching scheme and softstarting capability,” in Proc. IEEE Appl. Power Electron. Conf. (APEC), Feb. 2000, vol.1, pp. 111–118.

[138] K. Wang, C. Y. Lin, L. Zhu, D. Qu, F. C. Lee, and J. S. Lai, “Bidirectional dc-to-dc converters for fuel cell systems,” in Proc. IEEE Power Electron. in Transportation Conf., Oct. 1998, pp. 47–51.

[139] S. Han and D. M. Divan, “Dual active bridge buck-boost converter,” in Proc. IEEE Energy Conversion Congr. Expo. (ECCE), Sept. 2009, pp. 2905–2911.

[140] Hepp, Aloysius F., et al. "Batteries for aeronautics and space exploration: Recent developments and future prospects." Lithium-Sulfur Batteries (2022): 531-595.

[141] J. Walter and W. W. De Doncker, “High-power galvanically isolated dc-dc converter topology for future automobiles,” in Proc. IEEE Power Electronics Specialist Conf. (PESC), June 2003, vol. 1, pp. 27–32.

[142] F. Krismer, J. Biela, and J. W. Kolar, “A comparative evaluation of isolated bidirectional dc/dc converters with wide input and output voltage range,” in Proc. IEEE Ind. Appl. Conf. (IAS), Oct 2005, vol. 1, pp. 599–606.

[143] S. Hosseini, S. K. Haghighian, S. Danyali, and H. Aghazadeh, "Multi-input dc boost converter supplied by a hybrid PV/Wind turbine power systems for street lighting application connected to the grid," in Universities Power Engineering Conference (UPEC), 2012 47th International, 2012, pp. 1-6.

[144] Qin Lijun, Lu Xiao. EngineeringMatlab/Simulink-Based Research on Maximum Power Point Tracking of Photovoltaic Generation,2012 International Conference on Applied Physics and Industrial Engineering, Science Direct, Physics Procedia, 24; 2012. pp. 10–18.

[145] Lim Yan Hong, Hamill.Simple DC. Maximum power point Tracker for photovoltaic arrays. Electron Lett 2000;36(11):997–9.

[146] Kouro, Samir, et al. "Grid-connected photovoltaic systems: An overview of recent research and emerging PV converter technology." IEEE Industrial Electronics Magazine 9.1 (2015): 47-61.

[147] Khateb Ahmad H, Rahim Nasrudin Abd, Selvaraj Jeyraj, Williams Barry W. DCto-DC converter with low input current ripple for maximum photovoltaic power extraction. IEEE Trans Ind Electron 2015;62(4):2246–56.

[148] Anthon Alexander, Zhang Zhe, Anderson MichaelAE. A high power boost converter for PV systems operating up to 300 kHz using SiC devices. In: Proceedings of the IEEE International Power Electronics and Application Conference and Exposition:302-307; 2014.

[149] Li W, He X. Review of nonisolated high-step-up DC/DC converters in photovoltaic grid-connected applications. IEEE Trans Ind Electron 2011;58(4):1239–50.

[150] Benavides ND, Chapman PL. Modelling the effect of voltage ripple on the power output of photovoltaic modules. IEEE Trans Ind Electron 2008;55(7):2638–43.

[151] Poshtkouhi S, Palaniappan V. A general approach for quantifying the benefit of distributed power electronics for fine grained MPPT in photovoltaic applications using 3-D modeling. IEEE Trans Power Electron 2012;27(11):4656–66.

[152] Rajesh R, Carolin Mabel M. A comprehensive review of photovoltaic systems. Renew Sustain Energy Rev 2015;51:231–48.

[153] Emilio Mamarelis, Giovanni Petrone, Giovanni Spagnuolo. Design of a slidingmode-controlled SEPIC for PV MPPT applications. IEEE Trans Ind Electron 2014;61:3387–98.

[154] Qun Zhao FC. Lee.High-efficiency,high step-up DC-DC converters. IEEE Trans Power Electron 2003;18(1):65–73.

[155] Young-Ho Kim, Young-Hyok Ji, Jun-Gu Kim, Yong-Chae Jung, Yuen Won Chung. A new control strategy for improving weighted efficiency in photovoltaic AC module-type interleaved flyback inverters. IEEE Trans Power Electron 2013;28:2688–99.

[156] de Melo Priscila Facco, Gules Roger, Romaneli Eduardo felix Ribeiro, Annunziato Rafael christiano. A modified SEPIC converter for high-power-factor rectifier and universal input voltage applications. IEEE Trans Power Electron 2010;25(2):310–21.

[157] Goyal, Veer Karan, and Anshuman Shukla. "Isolated DC–DC boost converter for wide input voltage range and wide load range applications." IEEE Transactions on Industrial Electronics 68.10 (2020): 9527-9539.

[158] D. Ertekin, "A high gain switched-inductor-capacitor DC-DC boost converter for photovoltaic-based micro-grid applications," in CSEE Journal of Power and Energy Systems.

[159] A. A. A. Radwan and Y. A.-R. I. Mohamed, “Linear active stabilization of converter-dominated DC microgrids,” IEEE Trans. Smart Grid, vol. 3, no. 1, pp. 203–216, Mar. 2012.

[160] Hasaneen, B. M., and Adel A. Elbaset Mohammed. "Design and simulation of DC/DC boost converter." 2008 12th International Middle-East Power System Conference. IEEE, 2008.

[161] Rosas-Caro, Julio C., et al. "A DC–DC multilevel boost converter." IET Power Electronics 3.1 (2010): 129-137.

[162] Hwu, K. I., and Y. T. Yau. "High step-up converter based on charge pump and boost converter." IEEE Transactions on Power Electronics 27.5 (2011): 2484-2494.

[163] N. de Paula, D. de Castro Pereira, W. J. de Paula and F. L. Tofoli, "An extensive review of nonisolated DC-DC boost-based converters," 2014 11th IEEE/IAS International Conference on Industry Applications, Juiz de Fora, Brazil, 2014, pp. 1-8.

[164] Kapat, Santanu, and Philip T. Krein. "A tutorial and review discussion of modulation, control and tuning of high-performance dc-dc converters based on small-signal and large-signal approaches." IEEE Open Journal of Power Electronics 1 (2020): 339-371.

[165] Karami, Zeinab, et al. "Hybrid model predictive control of DC–DC boost converters with constant power load." IEEE Transactions on Energy Conversion 36.2 (2020): 1347-1356.

[166] Kapat, Santanu, and Philip T. Krein. "A tutorial and review discussion of modulation, control and tuning of high-performance dc-dc converters based on small-signal and large-signal approaches." IEEE Open Journal of Power Electronics 1 (2020): 339-371.

[167] J. Yang, W.-H. Chen, and Z. Ding, “Disturbance observers and applications,” Trans. Inst. Meas. Control, vol. 38, no. 6, pp. 621–624, 2016.

[168] W.-H. Chen, J. Yang, L. Guo, and S. Li, “Disturbance-observer-based control and related methods – An overview,” IEEE Trans. Ind. Electron., vol. 63, no. 2, pp. 1083–1095, Feb. 2016.

[169] Wu, Yuheng, and Yongqiang Ye. "Internal model-based disturbance observer with application to CVCF PWM inverter." IEEE Transactions on Industrial Electronics 65.7 (2017): 5743-5753.

[170] M. Sitbon, S. Schacham, and A. Kuperman, “Disturbance observerbased voltage regulation of current-mode-boost-converter-interfaced photovoltaic generator,” IEEE Trans. Ind. Electron., vol. 62, no. 9, pp. 5776–5785, Sep. 2015.

[171] Y. Mousavi, G. Bevan, I. B. Kucukdemiral and A. Fekih, "Observer-Based High-Order Sliding Mode Control of DFIG-Based Wind Energy Conversion Systems Subjected to Sensor Faults," in IEEE Transactions on Industry Applications, vol. 60, no. 1, pp. 1750-1759, Jan.-Feb. 2024.

[172] Q.-C. Zhong and D. Rees, “Control of uncertain LTI systems based on an uncertainty and disturbance estimator,” ASME J. Dyn. Syst. Meas. Control, vol. 126, pp. 905–910, 2004.

[173] T. Chandrasekhar and L. Dewan, “Sliding mode control based on TDC and UDE,” Int. J. Inf. Syst. Sci., vol. 3, no. 1, pp. 36–53, 2007.

[174] Y. Zhu and S. Zhu, “Adaptive sliding mode control based on uncertainty and disturbance estimator,” Math. Probl. Eng., vol. 2014, 2014, Art. no. 982101.

[175] S. E. Talole and S. B. Phadke, “Model following sliding mode control based on uncertainty and disturbance estimator,” J. Dyn. Sys. Meas. Control, vol. 130, no. 3, pp. 34501–5, 2008.

[176] Talole and S. Phadke, “Robust input-output linearization using uncertainty and disturbance estimation,” Int. J. Control, vol. 82, no. 10, pp. 1794–1803, 2010.

[177] Aharon, Ilan, Doron Shmilovitz, and Alon Kuperman. "Uncertainty and disturbance estimator-based controllers design under finite control bandwidth constraint." IEEE Transactions on Industrial Electronics 65.2 (2017): 1439-1449.

[178] Van Giap, Nam, et al. "Disturbance and uncertainty rejection-based on fixed-time sliding-mode control for the secure communication of chaotic systems." IEEE Access 9 (2021): 133663-133685.

[179] Wu, Yuheng, et al. "Uncertainty and disturbance estimator-based robust tracking control for dual-active-bridge converters." IEEE Transactions on Transportation Electrification 6.4 (2020): 1791-1800.

[180] W.-H. Chen, K. Ohnishi, and L. Guo, "Advances in disturbance/uncertainty estimation and attenuation," IEEE Trans. Ind. Electron., vol. 62, no. 9, pp. 5758–5762, Sep. 2015.

[181] Ojeda-Rodríguez, Á.; González-Vizuete, P.; Bernal-Méndez, J.; Martín-Prats, M.A. A Survey on Bidirectional DC/DC Power Converter Topologies for the Future Hybrid and All Electric Aircrafts. Energies 2020, 13, 4883.

[182] Iqbal, M.T.; Maswood, A.I.; Yeo, K.; Tariq, M. Dynamic Model and Analysis of Three phase YD Transformer Based Dual Active Bridge Using Optimised Harmonic Number for Solid State Transformer in Distributed System. In Proceedings of the 2018 IEEE Innovative Smart Grid Technologies—Asia (ISGT Asia), Singapore, 22–25 May 2018; IEEE: New York, NY, USA, 2018; pp. 523–527.

[183] Inoue, S.; Akagi, H. A Bidirectional DC–DC Converter for an Energy Storage System with Galvanic Isolation. IEEE Trans. Power Electron. 2007, 22, 2299–2306.

[184] Tan, Nadia Mei Lin, Takahiro Abe, and Hirofumi Akagi. "Design and performance of a bidirectional isolated DC–DC converter for a battery energy storage system." IEEE Transactions on Power Electronics 27.3 (2011): 1237-1248.

[185] Li, G.; Xia, J.; Wang, K.; Deng, Y.; He, X.; Wang, Y. Hybrid Modulation of Parallel-Series LLCLLC. Resonant Converter and Phase Shift Full-Bridge Converter for a Dual-Output DC–DC Converter. IEEE J. Emerg. Sel. Top. Power Electron. 2019, 7, 833–842.

[186] Jung, J.H.; Kim, H.S.; Ryu, M.H.; Baek, J.W. Design Methodology of Bidirectional CLLC Resonant Converter for High-Frequency Isolation of DC Distribution Systems. IEEE Trans. Power Electron. 2013, 28, 1741–1755.

[187] Chen, W.; Rong, P.; Lu, Z. Snubberless Bidirectional DC–DC Converter with New CLLC Resonant Tank Featuring Minimized Switching Loss. IEEE Trans. Ind. Electron. 2010, 57, 3075–3086.

[188] Bakeer, A.; Chub, A.; Blinov, A.; Lai, J.-S. Wide Range Series Resonant DC-DC Converter with a Reduced Component Count and Capacitor Voltage Stress for Distributed Generation. Energies 2021, 14, 2051.

[189] Li, X.; Bhat, A.K.S. Analysis and Design of High-Frequency Isolated Dual-Bridge Series Resonant DC/DC Converter. IEEE Trans. Power Electron. 2010, 25, 850–862.

[190] Tuan, C.A.; Takeshita, T. Analysis of Unidirectional Secondary Resonant Single Active Bridge DC–DC Converter. Energies 2021, 14, 6349.

[191] Demetriades, G.D.; Nee, H.P. Characterisation of the Soft-switched Single-Active Bridge Topology Employing a Novel Control Scheme for High-power DC-DC Applications. In Proceedings of the 2005 IEEE 36th Power Electronics Specialists Conference, Dresden, Germany, 16 June 2005; pp. 1947–1951.

[192] Ting, Y.; de Haan, S.; Ferreira, J.A. Efficiency improvements in a Single Active Bridge modular DC-DC converter with snubber capacitance optimization. In Proceedings of the IEEE International Power Electronics Conference (IPEC-Hiroshima 2014—ECCE ASIA), Hiroshima, Japan, 17 August 2014; pp. 2787–2793.

[193] Ting, Y.; De Haan, S.; Ferreira, J.A. The partial-resonant single active bridge DC-DC converter for conduction losses reduction in the single active bridge. In Proceedings of the 2013 IEEE ECCE Asia Downunder, Melbourne, VIC, Australia, 3–6 June 2013; pp. 987–993.

[194] Park, K.; Chen, Z. Open-circuit fault detection and tolerant operation for a parallel-connected SAB DC-DC converter. In Proceedings of the 2014 IEEE Applied Power Electronics Conference and Exposition—APEC, Fort Worth, TX, USA, 16–20 March 2014; pp. 1966–1972.

[195] Averberg, A.; Mertens, A. Characteristics of the single active bridge converter with voltage doubler. In Proceedings of the 2008 13th International Power Electronics and Motion Control Conference, Poznan, Poland, 1–3 September 2008; pp. 213–220.

[196] Fontana, C.; Forato, M.; Bertoluzzo, M.; Buja, G. Design characteristics of SAB and DAB converters. In Proceedings of the 2015 Intl Aegean Conference on Electrical Machines & Power Electronics (ACEMP), 2015 Intl Conference on Optimization of Electrical & Electronic Equipment (OPTIM) & 2015 Intl Symposium on Advanced Electromechanical Motion Systems (ELECTROMOTION), Side, Turkey, 21 August 2015; pp. 661–668.

[197] Fontana, C.; Forato, M.; Kumar, K.; Outeiro, M.T.; Bertoluzzo, M.; Buja, G. Soft-switching capabilities of SAB vs. DAB converters. In Proceedings of the IECON 2015 41st Annual Conference of the IEEE Industrial Electronics Society, Yokohama, Japan, 9–12 November 2015; pp. 003485–003490.

[198] M. C. Lee, C. Y. Lin, S. H. Wang, and T. S. Chin, “Soft-magnetic Febased nano-crystalline thick ribbons,” IEEE Trans. Magn., vol. 44, no. 11, pp. 3836–3838, Nov. 2008

[199] A. R. Alonso, J. Sebastian, D. G. Lamar, M. M. Hernando, and A. Vazquez, “An overall study of a dual active bridge for bidirectional dc/dc conversion,” in Proc. IEEE Energy Convers. Congr. Expo., 2010, pp. 1129–1135.

[200] C. Mi, H. Bai, C. Wang, and S. Gargies, “Operation, design and control of dual H-bridge-based isolated bidirectional dc-dc converter,” IET Power Electron., vol. 1, no. 4, pp. 507–517, Apr. 2008.

[201] Zhao, Biao, et al. "Overview of dual-active-bridge isolated bidirectional DC–DC converter for high-frequency-link power-conversion system." IEEE Transactions on power electronics 29.8 (2013): 4091-4106.

[202] H. S. H. Chung, W. L. Cheung, and K. S. Tang, “A ZCS bidirectional flyback dc/dc converter,” IEEE Trans. Power Electron., vol. 19, no. 6, pp. 1426–1434, Nov. 2004.

[203] A. A. Aboulnaga and A. Emadi, “Performance evaluation of the isolated bidirectional Cuk converter with integrated magnetics,” in Proc. 35th IEEE Annu. Power Electron. Spec. Conf., 2004, pp. 1557–1562.

[204] B. Zhao, Q. Yu, Z. Leng, and X. Chen, “Switched Z-source isolated bidirectional dc-dc converter and its phase-shifting shoot through bivariate coordinated control strategy,” IEEE Trans. Ind. Electron., vol. 59, no. 12, pp. 4657–4670, Dec. 2012.

[205] T. Hirose and H. Matsuo, “A consideration of bidirectional superposed dual active bridge dc-dc converter,” in Proc. 2nd IEEE Int. Symp. Power Electron. Distrib. Generation Syst., 2010, pp. 39–46.

[206] L. Zhu, “A novel soft-commutating isolated boost full-bridge ZVS-PWM dc-dc converter for bidirectional high power applications,” IEEE Trans. Power Electron., vol. 21, no. 2, pp. 422–429, Mar. 2006.

[207] R. W. A. A. D. Doncker, D. M. Divan, and M. H. Kheraluwala, “A threephase soft-switched high-power-density dc/dc converter for high-power applications,” IEEE Trans. Ind. Appl., vol. 27, no. 1, pp. 63–73, Jan./Feb. 1991

[208] M. H. Kheraluwala, R. W. Gascoigne, D. M. Divan, and E. D. Baumann, “Performance characterization of a high-power dual active bridge dc-todc converter,” IEEE Trans. Ind. Appl., vol. 28, no. 6, pp. 1294–1301, Nov./Dec. 1992.

[209] M. H. Kheraluwala and R. W. D. Doncker, “Single phase unity power factor control for dual active bridge converter,” in Proc. IEEE Ind. Appl. Soc. Annu. Meet., 1993, pp. 909–916.

[210] M. Kashif, “Bidirectional flyback dc-dc converter for hybrid electric vehicle: Utility, working and PSPICE computer model,” in Proc. Asia Pacific Conf. Postgraduate Res. Microelectron. Electron., 2012, pp. 61– 66.

[211] D. M. Bellur and M. K. Kazimierczuk, “Isolated two-transistor zeta converter with reduced transistor voltage,” IEEE Trans. Circuits Syst. II: Exp. Briefs., vol. 58, no. 1, pp. 41–45, Jan. 2011.

[212] S. Inoue and H. Akagi, “A bidirectional dc-dc converter for an energy storage system with galvanic isolation,” IEEE Trans. Power Electron., vol. 22, no. 6, pp. 2299–2306, Nov. 2007.

[213] G. G. Oggier, M. Ordonez, J. M. Galvez, and F. Luchino, “Fast transient boundary control and steady-state operation of the dual active bridge converter using the natural switching surface,” IEEE Trans. Power Electron., vol. 29, no. 2, pp. 946–957, Feb. 2014.

[214] H. Bai, C. Mi, and S. Gargies, “The short-time-scale transient processes in high-voltage and high-power isolated bidirectional dc-dc converters,” IEEE Trans. Power Electron., vol. 23, no. 6, pp. 2648–2656, Nov. 2008.

APPENDIX. ISS

Table A1. ISS components

Module	Length	Module	Length
Zarya	12.8 m	Node 2	6.1 m
Unity	5.5 m	Columbus	6.9 m
Zveda	13.1 m	Experiments Logistics Module (ELM) Pressurized Section (PS)	3.9 m
Z1 truss	4.6 m	Soyuz	7 m
P6 Truss	18.3 m	Dextre	3.5 m
Solar Array	73.2 m	Kibo	11.2 m
Destiny	8.5 m	S6 Truss	13.7 m
Canadarm 2	16.9 m	ELM Exposed Section	4.9 m
Quest Airlock	5.5 m	Kibo Exposed Facility	5.6 m
Pirs Airlock	4.9 m	Russian multi-purpose laboratory module	12.8 m
S0 Truss/ Mobile Transporter	13.4 m	Node 3	6.1 m
Mobile Base	5.8 m	Cupola	3 m
S1 Truss	13.7 m	Russian research module	12.8 m
P1 Truss	13.7 m	Progress	7.4 m
P3/P4 Truss	13.7 m	S5 Truss	3.3 m
P5 Truss	3.3 m	S3/S4 Truss	13.7 m

Note: These components have been launched from 1998-2009.

Table A2. ISS Loads

Load	Ch1 Net Power (W)	Ch2 Net Power (W)	Ch3 Net Power (W)	Ch4 Net Power (W)
Fan	1605	1605	535	1070
Battery Unit 1	6645	6645		
Atmosphere Controller	1200	1200		
Crew System	575	575		
Control System	820	820		
Communications	470	470		
Main Computer	385	385		
Robotic Workstation	8950	8950		
Canadian Robotic Arm	3210	3210		
Air Pump	1150	1150		
Lightning Bank 1	1080	1080		
Battery Unit 2			6645	6645
Lightning Bank 2			720	460
Experiment US 1			4250	
Experiment US 2				2275
Experiment US 3			2715	
Experiment US 4				2260

Note: Ch stands for ISS channels.